16 Cop.

EVALUATION OF CRITICAL FACTORS RELATED TO A
FLIGHT EXPERIMENT FOR REFLECTIVE SURFACE SAMPLES

prepared for

NATIONAL AERONAUTICS AND SPACE ADMINISTRATION

by

The Staff of the Optics Division and the Aerospace Electronics Division

GPO PRICE $ _____

OTS PRICE(S) $ _____

Hard copy (HC) 4.00

Microfiche (MF) 1.00

N65 15822
(ACCESSION NUMBER)   (THRU)

122
(PAGES)   (CODE)

CR 60400
(NASA CR OR TMX OR AD NUMBER)   14
                                     (CATEGORY)

EOS ELECTRO-OPTICAL SYSTEMS, INC.
300 N. HALSTEAD ST., PASADENA, CALIFORNIA

16 Cop.

16 Cop.

FINAL REPORT

EVALUATION OF CRITICAL FACTORS RELATED TO A FLIGHT EXPERIMENT FOR REFLECTIVE SURFACE SAMPLES

prepared for

NATIONAL AERONAUTICS AND SPACE ADMINISTRATION

by

The Staff of the Optics Division and the Aerospace Electronics Division

31 July 1964

Contract NAS 1-3850

NASA - Langley Research Center

Langley Station

Hampton, Virginia, 23365

E●S ELECTRO-OPTICAL SYSTEMS, INC.
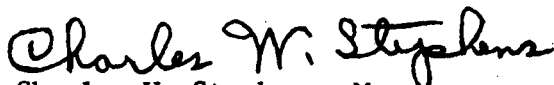300 N. HALSTEAD ST., PASADENA, CALIFORNIA

FOREWORD

This final report covers the program conducted from 23 March 1964 to 20 July 1964 on Contract NAS 1-3850. The work was performed at Electro-Optical Systems, Inc. by the staff of the Optics, Aerospace Electronics, and Product Assurance Divisions. The Project Manager was P. A. Button. The following persons assisted in the program and the preparation of this report: C. J. Campbell, D. P. Foote, R. E. Furlong, J. A. Geslin, R. P. Heile, D. G. Marlow, and C. D. Wilson. The program was under the direction of the Technical Monitor, Mr. Atwood R. Heath, Jr. of the NASA - Langley Research Center.

Reviewed and approved by

P. A. Button
Project Manager

Approved by

Charles W. Stephens, Manager
Optics Division

5101-Final

ABSTRACT

15822

This final report for Contract NAS1-3850 covers the evaluation
of critical factors related to a flight experiment involving reflective
surface samples. The program included the design, fabrication, and
test of a prototype rotating arm reflectometer and evaluation of this
approach for application to the flight experiment. Also reported are
the results of studies for operating bearings and seals in space,
valving for satellite control, and a general reliability analysis for
the satellite. Further studies regarding methods of separating causes
of sample degradation also are included.

CONTENTS

Contents (contd)

Contents (contd)

ILLUSTRATIONS

TABLES

1. INTRODUCTION

The quality of the reflectivity of solar concentrators reflective surfaces is an important factor in the efficiency and effectiveness of a solar power system. In the case of a solar power system designed to operate in space the reflecting surface of the solar collector must be exposed to the space environment and oriented towards the sun. There is much concern regarding the performance of solar collector reflective surfaces in the space environment. This is due to the meager data available concerning the space environment making it difficult to perform valid ground simulation tests and accurately assess the results.

As a result of this situation, it would be desirable to actually expose various solar concentrator reflective surfaces to the space environment for a period of time and measure their performance. Electro-Optical Systems, Inc. under Contract NAS 1-2880 performed a study to determine the feasibility of performing this solar concentrator reflective surface flight experiment. Among other things, this study program resulted in a conceptual design of a reflectometer to measure solar collector sample performance in the space environment.

The purpose of the program reported on in this document is to design and construct a rotating arm reflectometer and to evaluate its feasibility with respect to the design approach and its effectiveness in meeting the experiment requirements. A rotating arm reflectometer was constructed and evaluated. Since the instrument is a prototype it was designed for some flexibility with respect to the optical and electronic systems. Thus, various modifications to the basic approach of the rotating arm reflectometer may be made, if desired. In addition to the prototype reflectometer development, four other study subtasks were accomplished. These were; 1, an evaluation of the reliability of operating bearings and seals in space; 2, the problem of valving

for attitude control; 3, a reliability estimate for the overall solar
collector test satellite; and 4, further work in attempting to separate
the causes of reflector degradation in the space environment.

The duration of this program was approximately 16 weeks. This
report gives the results of all five subtasks.

2. SUMMARY AND RECOMMENDATIONS

This section summarizes the program for the evaluation of critical factors related to a flight experiment for reflective surface samples. The program was divided into five tasks and these were:

1. Demonstration model of optical system (reflectometer)
2. Bearings and seals for operation in space
3. Valving for attitude control
4. Reliability
5. Separation of effects.

The first task involved design, fabrication, and test whereas tasks 2 through 5 were studies. The five tasks are summarized in the following subsections.

2.1 Reflectometer

A full scale, rotating arm reflectometer was designed, fabricated, and tested. The design philosophy of the reflectometer was to provide a basic structure which would allow flexibility for the optical and electronic subsystems. Thus, modification can be made to the optical system (with the exception of the rotating arm) and electronics without a basic mechanical re-design and fabrication.

The basic instrument is a cylinder 20.5" in diameter and 6.5" high. The rotating arm, which contains two front surface mirrors, scans a ring of samples located on a 9" radius. Using circular samples, 1.5" in diameter, a total of 28 samples and two calibrate positions can be accommodated. Only seven samples are provided on the demonstration model. Six of these have electroformed nickel substrates and have a variety of coatings. The other sample is an optical flat for evaluation purposes.

The optics of the reflectometer consists of two separate optical systems each using the optics of the rotating arm. One optical system utilizes a miniature incandescent filament for the light source, a collimating and field lens, two beamsplitters, and a 2 x 2 mm lead sulfide detector to perform a single "white light" reflectance measurement. The other optical system uses the virtual image of the sun (formed by a spherical convex reflector) for the light source. Light enters the instrument through a fused quartz window. The light traverses this optical system in a manner similar to the first optical system up to the last beamsplitter. Here the light enters a 60° prism. At the second face of this prism a portion of the light is refracted and dispersed into a spectrum. The other portion of the light is reflected from the second prism and passes out the third face in an undispersed form giving a "white light" reflectance measurement. Four adjacent 4 x 4 mm lead sulfide detectors are used to measure the spectral energy. These four detectors cover the wavelength regions of 0.38 - 0.46 μ, 0.46 - 0.62 μ, 0.62 - 1.06 μ and 1.06 - 1.75 μ with fairly good spectral resolution especially at low wavelengths. The astigmatic image formed by the sunlight reflectivity off the spherical reflector is focussed on the detectors to provide the spectral resolution. The white light is a 2 x 2 mm lead sulfide cell.

Both optical systems are calibrated by means of a 45°-90°-45° prism which makes use of total internal reflection. This prism is located in one of the sample positions. All transmitting elements of the solar virtual image optical system are fused quartz. All detectors use a bridge network with a dc amplifier. The arm rotates at 24 rpm.

Both "white light" detectors can tolerate sample misalignment of about $\pm$ 1°. The solar virtual image optical system can tolerate a satellite misorientation of about $\pm$ 4°. The drift on the detector with the highest gain (worst conditions) will produce a 0.1% reflectance error. Noise is no problem and all detectors exhibit clean signals. All detector outputs can easily be in the 0 - 5 volt range. The output

of the uv detector was low because of the greater atmospheric absorption. However, in space this problem is removed. The largest problem encountered is the curvature of the samples. This curvature (about -100" focal length) destroys the resolution of the spectral measurements. It is recommended that a different approach be used to overcome this problem.

This approach could use a field lens immediately behind the last beamsplitter. This would form an image of the sample (similar to the "white light" optical system) which could be used as the entrance "slit" to the spectrometer. The advantage here is that the entrance "slit" is spatially stable and its position is less sensitive to sample misalignment and curvature.

In order to minimize drift problems (which is a problem only in meeting the 0 - 5 volt telemetry requirements) it is recommended that a modification be made to the electronic system. This could take the form of light chopping via reflectometer arm rotation or ac coupling.

2.2 Bearings and Seals for Operation in Space

As a result of the study performed on the problem of bearings and seals for operation in space it is felt that the most reliable solution is to utilize pressurized bearings operating through a seal. The bearing lubricant would be methyl-phenyl-silicone oil with a dye thickener. The seal would be a standard metal bellows type unit and the sealing surface would be coated with molybdenum disulfide in a sodium silicate binder. The mating ring would be a sintered mixture of silver (80%) and MoS_2 (20%).

2.3 Valving for Attitude Control

Various valve manufacturers were contacted and, as a result, it is felt that state-of-the-art valves (such as in OSO) will satisfy the leak rate requirements of the solar collector test satellite.

2.4 Reliability

A modest reliability analysis was made on the overall test satellite (not just the reflectometer). This analysis included a gross parts count and failure rate assessment, the various failure modes and effects, and a reliability optimization. The result of the mean-time-to-failure computation is that the probability of the total satellite operating successfully for one year is 56%. The weakest link in the chain appears to be the command receiver.

2.5 Separation of Effects

Further data on micrometeoroids and low energy protons are given. It is concluded that it would be extremely difficult to separate the effects of low energy protons and micrometeoroids with one satellite. Two approaches to separating the above effects were analyzed. The most promising is a spatial approach where an orbit is chosen with the peak proton flux and the peak micrometeoroid flux occurring in different portions of the orbit. By means of a movable shield, one set of samples can be given more proton exposure while another set is given more micrometeoroid exposure.

3. DEMONSTRATION MODEL OF OPTICAL SYSTEM

This section describes the work accomplished in the design, fabrication, and testing of the demonstration model of the optical system (reflectometer). Figure 3.1 shows the assembled reflectometer and the heliostat accessory. The basic configuration of the reflectometer is similar to the preferred experiment package described in the contract NAS 1-2880 final report. The purpose of the reflectometer is to verify overall feasibility with particular attention to:

1. Adequate signal-to-noise ratio
2. Stability
3. Insensitivity to alignment.

The philosophy of the instrument design was to provide a basic structure for the rotating arm reflectometer concept and yet provide flexibility in the optical system design. In this respect, the instrument is not an end in itself in that, at later dates, the optical system can be modified (with the exception of the rotating arm) to evaluate other approaches. As a result, little attention was given to minimizing the weight and volume of the optical system. However, the actual operation of the reflectometer in the space environment was considered in the design and this is evidenced by the use of fused quartz optical elements, singlet optical elements, windows for simulated sealing conditions, and considerations of satellite attitude control accuracy. Thus, the reflectometer described in this section is a step towards an instrument which would measure the reflectance degradation of solar concentrator reflective surfaces in the space environment. The following subsections describe the mechanical, optical, and electronic aspects of the reflectometer and also the test results.
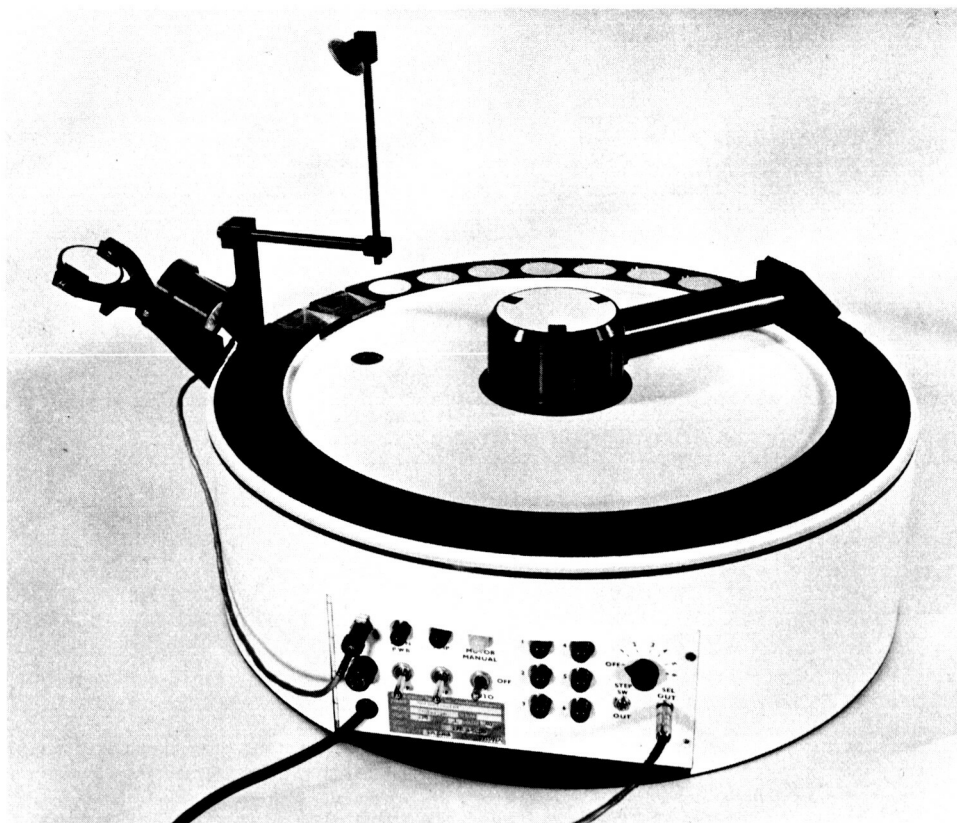
FIG. 3-1 REFLECTOMETER AND HELIOSTAT

3.1 Mechanical

The mechanical aspects of the reflectometer consist of the basic structure, the rotating arm assembly, the optical and electronic mounting bracketry, and the heliostat.

3.1.1 Basic Structure

The basic structure of the reflectometer is shown in EOS Engineering Drawing No. 5101-1 (enclosed). The structure consists of two machined aluminum discs separated 5-1/2 inches apart by four standoffs. The diameter of the structure is such that 28 samples (1-1/2 inches in diameter) and 2 calibrate positions could be accommodated. The samples are mounted on the periphery of the upper disc in the appropriate holes provided. It was felt that it was not necessary to have a complete ring of samples for the purposes of the demonstration reflectometer. As a result, only seven samples are mounted on the reflectometer covering an arc of a little less than 90°. In addition, provision has been made to mount two calibrate prisms and one 0% calibrate position. The samples themselves are mounted in cups which are capable of individual alignment. The upper structural disc has a central hole which accommodates the rotating arm assembly. A smaller hole in the upper disc allows the sunlight to enter the instrument for use as a light source. The lower structural disc provides a mounting surface for all of the electronic components and a majority of the optical components. A thin aluminum skirt fits around the two structural discs and serves to keep out stray light and dust. A cutout is provided in the skirt for the control panel. The instrument rests on four rubber pads fastened to the bottom of the lower disc.

3.1.2 Rotating Arm Assembly

The rotating arm assembly provides the motion which scans the reflectometer beam of light across the samples. It consists of a hollow cylindrical section and a hollow cylindrical tube whose axes are perpendicular to each other. The cylindrical section mounts in the center hole of the upper structural disc. This section contains

two bearings three inches apart which provide the arm rotation. At
the bottom of this section is a disk which provides a surface
for driving purposes. The rotating arm assembly provides mounting and
adjustments for two mirrors and mounting for one quartz window.

3.1.3 Optical Element Mounting

All optical elements are mounted on the lower struc-
tural disc with the exception of the two mirrors and one window in the
rotating arm assembly and the one window where solar radiation enters
the instrument. A single mirror is located directly below the rotating
arm assembly cylindrical section and is provided with a push-pull type
angular adjustment. The two collimating lenses and beam splitters (see
Section 3.2) are mounted in a non-adjustable integral unit. All other
optical elements are mounted in separate fixtures and are adjustable to
various degrees. Also, all optical elements are fastened with glue on
their mounting fixtures.

3.1.4 Electronic Component Mounting

The reflectometer is designed so that all electronic
component mounting is on the lower structural disc. The three main
areas of electronic component mounting are on the lower structural disc
and the outer and inner control panels. These control panels are mounted
in turn on the lower structural disc. The outer control panel is hinged
to permit access to the interior of the instrument for adjustment and
inspection. This panel can swing out from the instrument through the
cutout in the skirt. The inner control panel is located directly behind
the outer control panel and is mounted in a vertical position.

3.1.5 Heliostat

Since the reflectometer was to be tested using the sun
as a light source, it was felt necessary to construct a modest heliostat
to direct the sunlight at a fairly constant angle into the instrument.
The heliostat is mounted on the edge of the upper structural disc and
consists of a motor and two mirrors. The motor drives one mirror at the
rate of 1/2 revolution per day and directs the sunlight towards the

second mirror which is adjustable in height and reflects the sunlight into the instrument. Power for the heliostat motor is supplied from a receptacle located in the outer control panel. The heliostat is not an integral part of the reflectometer and may be easily removed and stowed in a separate case.

3.2 Optical

The optical portion of the reflectometer consists of two separate optical systems both sharing the optics of the rotating arm assembly. Two light sources are used (one for each optical system) which are an incandescent filament and a virtual image of the sun as formed by a convex spherical reflector. The spatial relations of the two optical systems are shown in Figures 3.2 and 3.3. Each optical system has a "collimating" lens which nearly collimates the beams as they traverse the rotating arm. The light beams of the incandescent light source (ILS) optical system and the solar virtual image (SVI) optical system have a common aperture stop at the sample. The optical axes of the ILS and SVI optical systems are tilted slightly (about 2°) with respect to (and on either side of) the normal to the sample. As a result, the collimated light of the ILS optical system passes through beamsplitter A, goes to the sample, and is reflected off beamsplitter B. On the other hand, the collimated light of the SVI optical system passes through beamsplitter B, goes to the sample, and is reflected off beamsplitter A. Thus, the two optical systems can be treated separately. The following subsections discuss the optics of the rotating arm assembly, the ILS and SVI optical systems, the calibrate functions, and the samples.

3.2.1 Rotating Arm Assembly

The rotating arm assembly contains two mirrors (M_4 and M_5 - Figure 3.2). Both mirrors accommodate the ILS and SVI optical systems. Since mirror M_3 also accommodates both optical systems, it will also be treated in this section. Mirrors M_3, M_4, and M_5 have

SPECTRAL
DETECTORS (4)

WHITE LIGHT DETECTOR

BEAM SPLITTERS

INCANDESCENT WHITE
LIGHT DETECTOR

SAMPLE

PRISM

M_1 AND M_2

INCANDESCENT LIGHT SOURCE

SPHERICAL CONVEX
REFLECTOR

(a) TOP VIEW (unfolded)

M_5

SAMPLE

M_4

M_3

COLLIMATING LENS

M_1

M_2

SPHERICAL
CONVEX
REFLECTOR
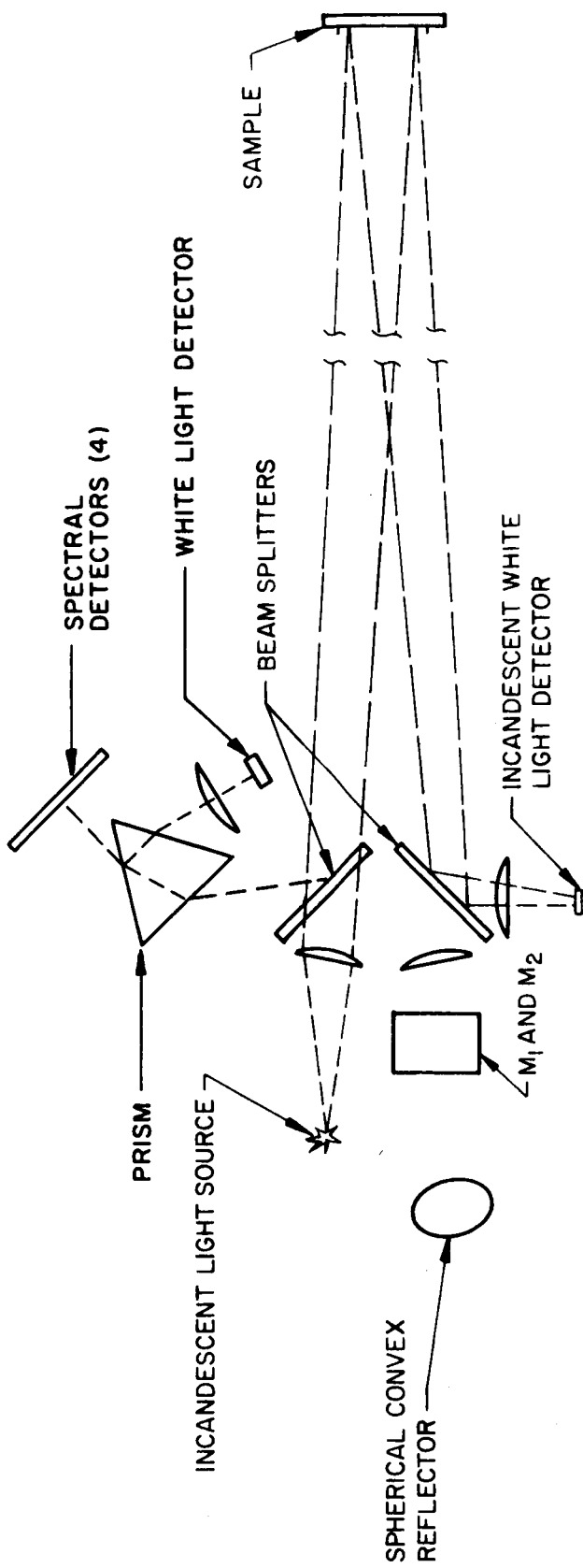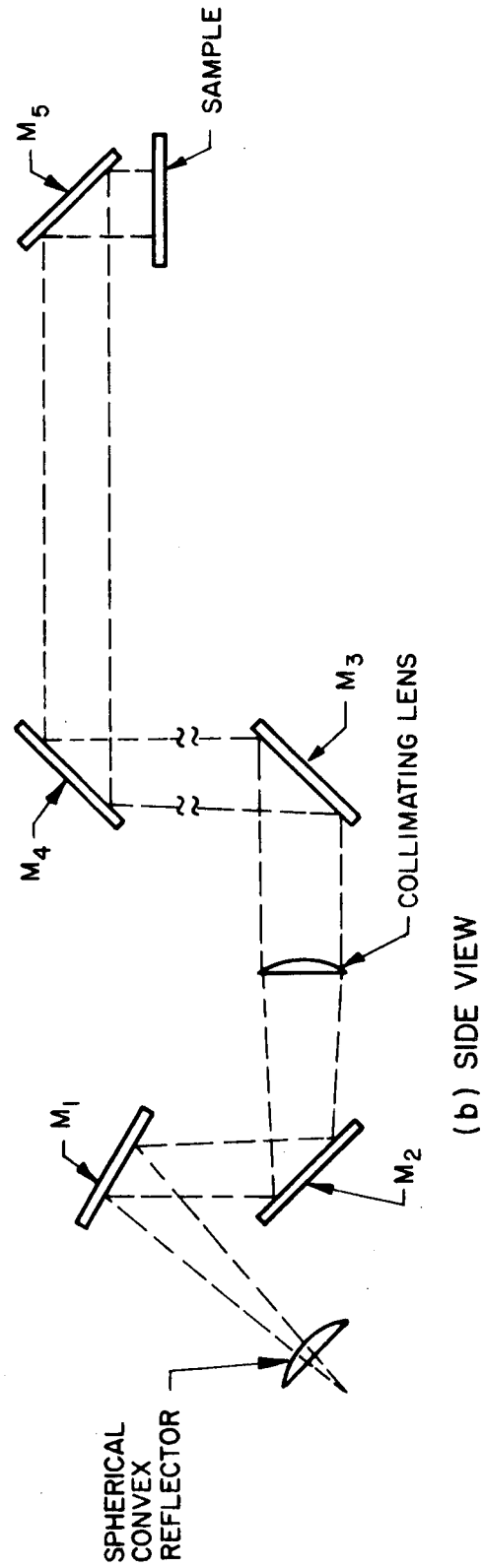
(b) SIDE VIEW

FIG. 3-2 REFLECTROMETER OPTICAL SYSTEM

FIG. 3-3   REFLECTOMETER, TOP REMOVED
            BACK VIEW

angular push-pull adjustments. All mirrors in the entire reflectometer optical system (including the heliostat) are front surface and coated with aluminum with no overcoat.

The rotating arm assembly also includes a quartz window 0.125" thick. The location of the window can be seen in EOS Engineering Drawing 5101-1 (enclosed). The window serves no functional purpose with respect to the reflectometer demonstration model other than to simulate a window which would be present on a satellite-borne instrument. The purpose of the window in the satellite-borne instrument is for sealing in the event that sealed bearings are used for the rotating arm assembly. The window is tilted (about 10°) so that the air (vacuum)/quartz interface reflection does not interfere with the reflectance measurement. This tilt (and window thickness) represents a beam displacement of 0.015" which is not serious with respect to vignetting. Also, the displacement is cancelled out when the beam returns through the window.

Mirrors M_3, M_4, and M_5 were aligned with the use of a gas CW laser. Alignment was initiated with just M_3 and not other optical elements present. The laser was adjusted so that its beam was parallel to and 0.75" above the lower structural disk. The optical axes of both the ILS and SVI systems and all detectors are 0.75" above this reference surface. Also, the laser beam bisected the angle between the optical axes of the two optical systems and impinged on the center of mirror M_3. A translucent screen with a cross-hair in the center was placed in the M_4 position and M_3 was adjusted until the laser beam was centered. Actually, when M_3 is properly aligned the laser beam is slightly off the center of the translucent screen due to the parallel-plate action of the quartz window. Under these conditions, when the reflectometer arm is rotated, the beam appears to rotate about the cross-hair. Mirror M_3 was adjusted until the radius of rotation of the beam is a minimum and centered on the cross-hair. Mirror M_4 was then installed and the translucent screen placed at M_5. Mirror M_4 was adjusted using the

same criteria. Mirror M_5 was installed and adjusted until the beam
was normal to the lower structural disk reference surface. This normal-
ity was determined by placing a flat reference mirror on the reference
surface and folding the beam back on itself. A screen with a hole the
size of the laser beam was placed over the laser and M_5 was adjusted
so the return beam coincided with the hole. This adjustment is quite
accurate because of the long optical lever arm (about 40"). The samples
and calibrate prisms can also be aligned in this manner.

The effect of bearing run-out on optical alignment
was also checked. The aligned rotating arm assembly was removed from
the top structural plate and mounted so that light from a collimator
was transmitted through the assembly. A flat mirror was placed over
the aperture just below M_5 so that the light was sent back to the
collimator. Finger pressure was applied to the end of the arm (the
non-rotating part of the assembly was held rigid) and the mechanical
misalignment was about 30 arc seconds. Since the combination of mirrors
M_4 and M_5 have retrodirective properties a bearing run-out misalignment
can only result in vignetting. Thus, the bearing run-out misalignment
is not serious.

3.2.2 Incandescent Light Source Optical System (ILS)

This section describes the incandescent light source
system and includes the light source, optical elements, and detector.
Optical system alignment and transmission are also discussed. The
purpose of the ILS optical system is to perform a single "white light"
(broad spectral band as determined by the spectral characteristics of
the light source, optical system, and detector) reflectance measurement
on the samples.

3.2.2.1 ILS Optical System

The ILS optical system is shown in Fig.'s 3.4 & 3.5.
The light source is a B&L tungsten filament bulb, catalog No. 71-71-44.
It draws 390 ma in a range of 1.5 to 2.5 volts. The collimating lens
has a 6 cm focal length and a 2 cm clear aperture. The collimating

FIG. 3-4 ILS OPTICAL SYSTEM

Labels in figure: SAMPLE, DETECTOR, IMAGE OF FILAMENT, FIELD LENS, QUARTZ BEAMSPLITTER, GLASS BEAMSPLITTER, COLLIMATING LENS, FILAMENT
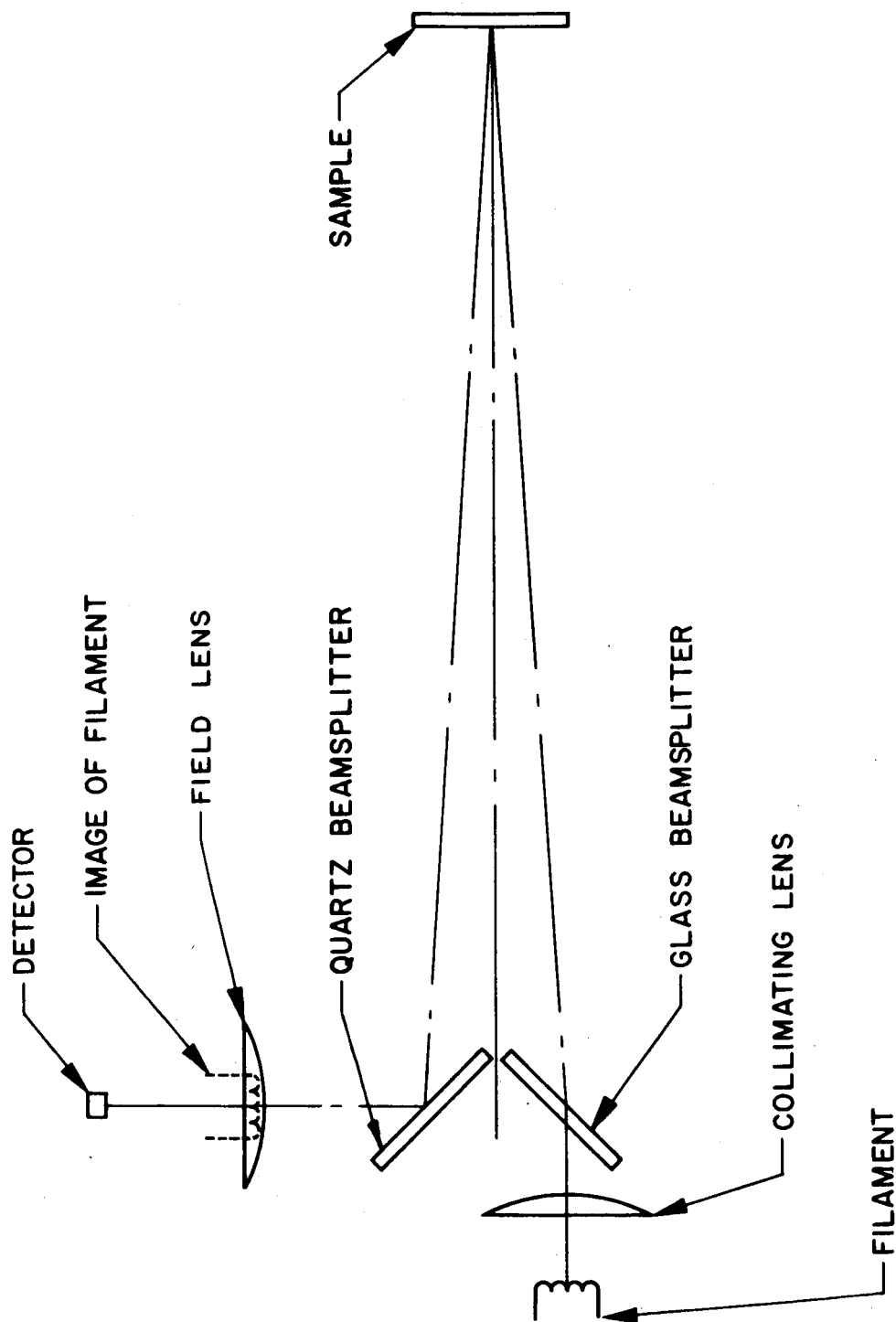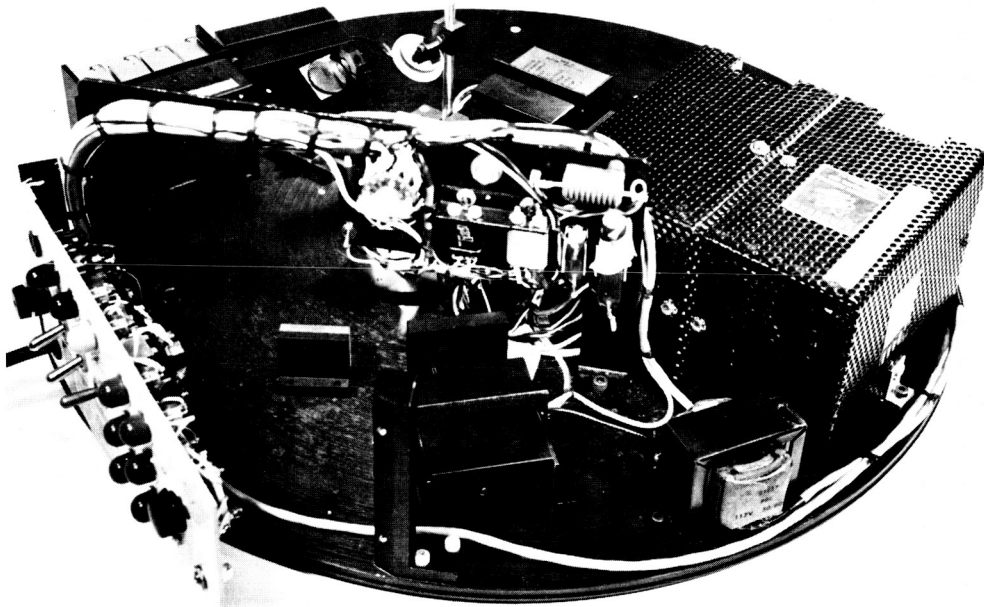
FIG. 3-5   REFLECTOMETER, TOP REMOVED
          FRONT VIEW

lens images the filament on the field lens. The field lens images
the sample on the detector. The detector is a 2 x 2 mm PbS element.
The beamsplitter which transmits the ILS light is glass and that which
reflects is quartz. The aluminum coating on both beamsplitters is on
the side towards the sample. The reason for two different materials
for the beamsplitters is economy. Since the incandescent filament is
very weak in the ultraviolet there is little need for quartz and all
ILS transmitting optics are glass. In the actual satellite-borne
instrument fused quartz would be used for its desirable resistance to
the space environment.

Because of sample alignment considerations
(Section 3.2.2.2) the actual size of the incandescent filament should
be as small as possible (as long as the signal level is acceptable).
The dimensions of the B&L source are ideal from this point of view.
However, the rated lifetime of this source leaves something to be
desired. One source (B&L) was life tested at 2.5 volts and burned out
at 84 hours. Even though the total one year on-time for the satellite-
borne instrument may be less than this, it would be desirable to operate
the source at a lower voltage. The B&L source gives satisfactory
signal levels when operated at 1.5 volts. This is 60% of its rated
voltage and according to the General Electric characteristic curves
of miniature tungsten filament lamps the 60% reduction of rated voltage
represents a 500x increase over the rated lifetime. This corresponds
to 42,000 hours which is more than sufficient. However, it is recom-
mended that some life testing be done on various lamps before the final
light source choice be made.

3.2.2.2 ILS System Alignment

The only element of the ILS optical system
which is capable of adjustment is the light source and this adjustment
is in x, y, and z. With the reflectometer arm over a sample the light
source is adjusted to focus its image at the field lens. The average
size of this image is 0.45 cm and the clear aperture of the field

lens is 2 cm. This means that the image may be displaced $\pm$ 0.77 cm due to sample misalignment and the light will still pass through the 2 cm clear aperture. Regardless of where the light passes through the clear aperture all the light will impinge on the detector since the field lens images the sample on the detector. The optical distance from the sample to the field lens is about 45 cm and the tangent of the displacement angle is 0.77/45 = 0.018 or an angle of 1°. Thus, the ILS optical system can tolerate a sample misalignment of $\pm$ 1° and still make a valid reflectance measurement. This sample misalignment tolerance can be increased by increasing the clear aperture of the field lens. This will also increase the dimensions of the rotating arm assembly to avoid vignetting.

The focal length of the single element plano-convex field lens is 4 cm and the detector is located about 4.5 cm from this lens. Thus, the ratio of the sample-field lens distance to the detector-field lens distance is 10. Since the detector area is 2 x 2 mm then this represents a 2 x 2 cm area on the sample that is seen by the detector. However, the clear aperture of the collimating lens is 2 cm and the light between the collimating lens and sample is convergent so the light spot on the sample is less than 2 cm diameter. Thus, the image of the sample (light spot) on the detector will be smaller than the detector sensitive area resulting in all the light passing through the field lens impinging on the detector.

It was attempted to use all single element lenses in the ILS optical system for simplicity and ruggedness. However, only the field lens is a singlet. The collimating lens is a cemented doublet. A single element collimating lens was tried but the image size at the field lens was about 1.8 cm diameter due to spherical abberation over such a long path length. This left very little room for sample misalignment. Therefore, the satellite-borne instrument should have a cemented or air spaced doublet for the ILS optical system collimating lens.

3.2.2.3 Transmission

To evaluate the performance of the ILS optical system the transmission of the optical system should be determined. This determination should include all reflecting and refracting elements between the light source and the detector. Because of the large number of optical elements between the light source and detector, most of which are at 45° to the incident beam, the transmission evaluation should take into account polarization effects. Table 3.1 traces the light path from light source to detector (minus the sample which is to be measured) and lists all interfaces by optical element and type.

Interface	Optical Element	Type
1	Collimating lens	Transmission
2	Beamsplitter	Transmission
3	Mirror M_3 (Fig. 3.2)	Reflection
4	Quartz window	Transmission
5	Mirror M_4	Reflection
6	Mirror M_5	Reflection
Sample		
7	Mirror M_5	Reflection
8	Mirror M_4	Reflection
9	Quartz window	Transmission
10	Mirror M_3	Reflection
11	Beamsplitter	Reflection
12	Field lens	Transmission

TABLE 3.1   ILS OPTICAL SYSTEM INTERFACES

From Table 3.1 we can write the following expression for the transmission of the ILS optical system:

$$T = T_1 \times T_2 \times R_3 \times T_4 \times R_5 \times R_6 \times R_7 \times R_8 \times T_9 \times R_{10} \times R_{11} \times T_{12} \quad (3.1)$$

where T and R refer to transmission and reflection coefficients, respectively. However, the optical elements which are at 45° to the incident radiation have two transmission and reflection coefficients. These are for planes of polarization parallel and perpendicular to the plane of reflection or refraction and are usually identified by the subscripts p and s, respectively. Radiation from the light source can be considered as having two mutually perpendicular planes of polarization. Let the polarization direction V be normal to the lower structural disk of the reflectometer at the light source and H is in the direction parallel to the disk. Then, the transmission of the ILS optical system is

$$T = \frac{T_V + T_H}{2} . \quad (3.2)$$

The value of T will vary (by a known amount) as the reflectometer rotates. This is because the particular polarization reflection coefficients of the two mirrors in the rotating arm are a function of the arm angular position with respect to mirror M_3. An analysis has been carried out evaluating the ILS optical system transmission at arm positions of 0° and 90°. The 0° position occurs when mirror M_4 reflects the light parallel to the incident light on mirror M_3. Thus, Equation 3.1 can be more accurately written to account for polarization effects and arm position as

$$(3.3)$$

$$T_{V\ 0^\circ} = T_1 \times T_{2s} \times R_{3p} \times T_4 \times R_{5p} \times R_{6p} \times R_{7p} \times R_{8p} \times T_9 \times R_{10p} \times R_{11s} \times T_{12}$$

$$T_{V\ 90^\circ} = T_1 \times T_{2s} \times R_{3p} \times T_4 \times R_{5s} \times R_{6s} \times R_{7s} \times R_{8s} \times T_9 \times R_{10p} \times R_{11s} \times T_{12}$$

$$T_{H\ 0^o} = T_1 \times T_{2p} \times R_{3s} \times T_4 \times R_{5s} \times R_{6s} \times R_{7s} \times R_{8s} \times T_9 \times R_{10s} \times R_{11p} \times T_{12}$$

$$T_{H\ 90^o} = T_1 \times T_{2p} \times R_{3s} \times T_4 \times R_{5p} \times R_{6p} \times R_{7p} \times R_{8p} \times T_9 \times R_{10s} \times R_{11p} \times T_{12}$$

The polarization effects of the collimating lens, tilted quartz window and field lens are assumed to be negligible.

Equations 3.3 can be simplified by grouping common terms. Assume that the collimating lens, the quartz window, and the field lens are all quartz elements (which they would be in the satellite-borne instrument). In this case we may write

$$T_A^4 = T_1 \times T_4 \times T_9 \times T_{12} \tag{3.4}$$

where T_A is the transmission of one quartz element/air interface (actually two interfaces). Since all mirrors are aluminized we can write for this type of reflection, R_{Bp} and R_{Bs} where the subscript B refers to aluminum reflection at 45°. Finally, we can assign a subscript c to the beamsplitter. The result is

$$T_{V\ 0^o} = T_A^4 \times T_{cs} \times R_{Bp}^6 \times R_{cs}$$

$$T_{V\ 90^o} = T_A^4 \times T_{cs} \times R_{Bp}^2 \times R_{Bs}^4 \times R_{cs} \tag{3.5}$$

$$T_{H\ 0^o} = T_A^4 \times T_{cp} \times R_{Bs}^6 \times R_{cp}$$

$$T_{H\ 90^o} = T_A^4 \times T_{cp} \times R_{Bs}^2 \times R_{Bp}^4 \times R_{cp}$$

There are seven terms in Equations 3.5 to be evaluated – T_A, T_{cs}, T_{cp}, R_{cs}, R_{cp}, R_{Bs}, and R_{Bp}.

The amount of light reflected at one normal incident quartz/air interface is

$$R = \frac{(n-1)^2}{(n+1)^2}$$

The transmission for one interface is $T = 1-R$. Each quartz element has two interfaces so the total light transmitted is T^2 (ignoring secondary reflections, etc.). Thus, the term T_A is

$$T_A = \left[1 - \frac{(n-1)^2}{(n+1)^2} \right]^2 .$$

Table 3.2 (Ref. 1) gives refractive index data for fused quartz.

λ (μ)	n
0.34669	1.47757
0.404656	1.46971
0.435835	1.46677
0.546074	1.46014
0.643847	1.45676
1.01398	1.45030
1.12866	1.44893
1.36728	1.44622
1.52952	1.44434
1.6932	1.44234
1.81307	1.44078
1.97009	1.43861

TABLE 3.2   REFRACTIVE INDEX OF FUSED QUARTZ

The value of T_A at five different wavelengths is 0.927, 0.928, 0.932, 0.932, and 0.934 for wavelengths of 0.35, 0.40, 0.50, 0.70, and 1.00, respectively.

The two polarized reflection coefficients for the aluminized mirrors (R_{Bs} and R_{Bp}) may be calculated from the optical constants of aluminum. An approximation of this calculation is

$$R_{Bp} = \frac{(n - \frac{1}{\cos\phi})^2 + k^2}{(n + \frac{1}{\cos\phi})^2 + k^2} \tag{3.6}$$

$$R_{Bs} = \frac{(n - \cos\phi)^2 + k^2}{(n + \cos\phi)^2 + k^2}$$

where n and k are refractive index and absorption coefficients, respectively, and ϕ is angle of incidence. The validity of Equations 3.6 were checked by using a more exact expression (Ref. 2). This is

$$R_{Bs} = \frac{a^2 + b^2 - 2a\cos\phi + \cos^2\phi}{a^2 + b^2 + 2a\cos\phi + \cos^2\phi} \tag{3.7}$$

$$R_{Bp} = R_{Bs} \left[\frac{a^2 + b^2 - 2a\sin\phi\tan\phi + \sin^2\phi\tan^2\phi}{a^2 + b^2 + 2a\sin\phi\tan\phi + \sin^2\phi\tan^2\phi} \right]$$

where

$$a^2 = \frac{1}{2n_o^2} \left\{ \left[(n^2 - k^2 - n_o^2 \sin^2\phi)^2 + 4n^2k^2 \right]^{1/2} + n^2 - k^2 - n_o^2\sin^2\phi \right\}$$

and

$$b^2 = \frac{1}{2n_o^2} \left\{ \left[(n^2 - k^2 - n_o^2 \sin^2\phi)^2 + 4n^2k^2 \right]^{1/2} - n^2 + k^2 + n_o^2\sin^2\phi \right\}$$

where n_o is (in our case) 1.00. Figure 3.6 gives data on the optical constants of aluminum from various sources. There appears to be a discrepancy of reported absorption coefficients below 0.7 microns. The line curves were the values used for these calculations. Calculations were made using Equations 3.6 and 3.7 for $\phi = 45^o$. The values of R_{Bp} and R_{Bs} using Equation 3.6 are 0.895 and 0.944. These compare to 0.898 and 0.947 for R_{Bp} and R_{Bs}, respectively, as calculated from Equations 3.7. As a result of this good agreement the easier Equation 3.6 was used to calculate the polarization reflection coefficients shown in Fig. 3.7. Since optical constant data on aluminum is lacking in the 1.0 - 2.0 μ region (our region of spectral interest is from about 0.3 to 2.0 μ) the dashed portion of the R_{Bp} and R_{Bs} curves represent an interpolation (a data point at 2.0 μ (Ref. 3) gives $n = 2.3$ and $k = 16.5$) aided by the normal incidence curve (Ref. 7).

Finally, the beamsplitter values R_{cp}, R_{cs}, T_{cp}, and T_{cs} are needed for the ILS system transmission calculation. Figure 3.8 shows unpolarized transmission values for the two beamsplitters used in the prototype reflectometer. These were measured on a Beckman DU spectrophotometer at 45° incidence and include interface losses. The data are not for the two polarization angles, thus, their use for the R_{cp}, R_{cs}, T_{cp}, and T_{cs} terms is an approximation. However, in view of the large number of optical interfaces in the ILS optical system an approximation on one does not seem serious.

Using Equations 3.5 the polarization transmission coefficients for the ILS optical system can be calculated (Table 3.3).

λ (μ)	$V_0{}^o$	$V_{90}{}^o$	$H_0{}^o$	$H_{90}{}^o$
0.35	0.0332	0.0392	0.0425	0.0353
0.40	0.0354	0.0425	0.0466	0.0383
0.50	0.0349	0.0432	0.0484	0.0391
0.70	0.0253	0.0349	0.0411	0.0299
1.00	0.0415	0.0510	0.0565	0.0460

TABLE 3.3 POLARIZATION TRANSMISSION COEFFICIENTS
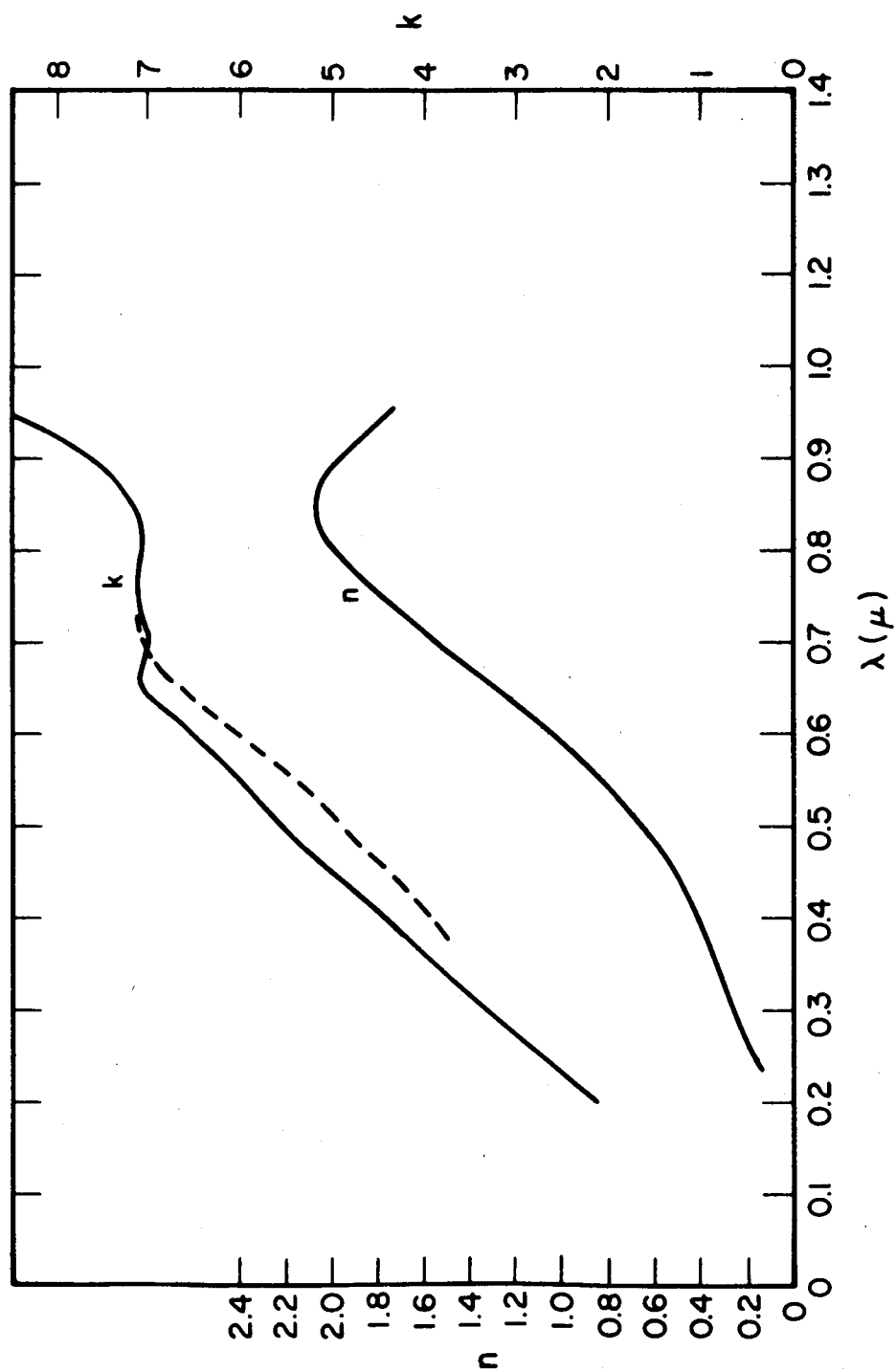
FIG. 3-6 OPTICAL CONSTANTS OF ALUMINUM (Ref. 3, 4, 5, 6)
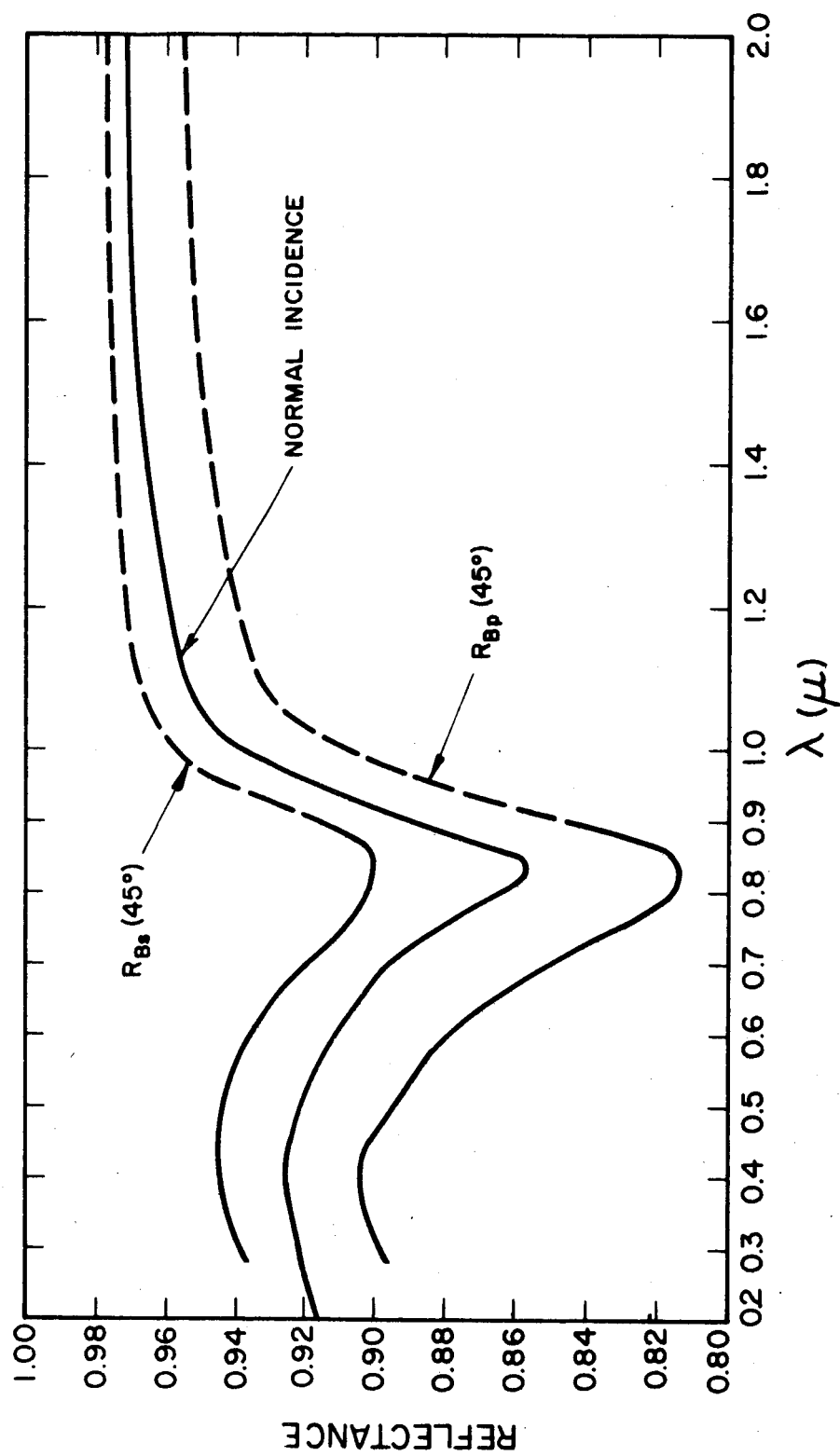
FIG. 3-7 POLARIZATION REFLECTION COEFFICIENTS FOR ALUMINUM
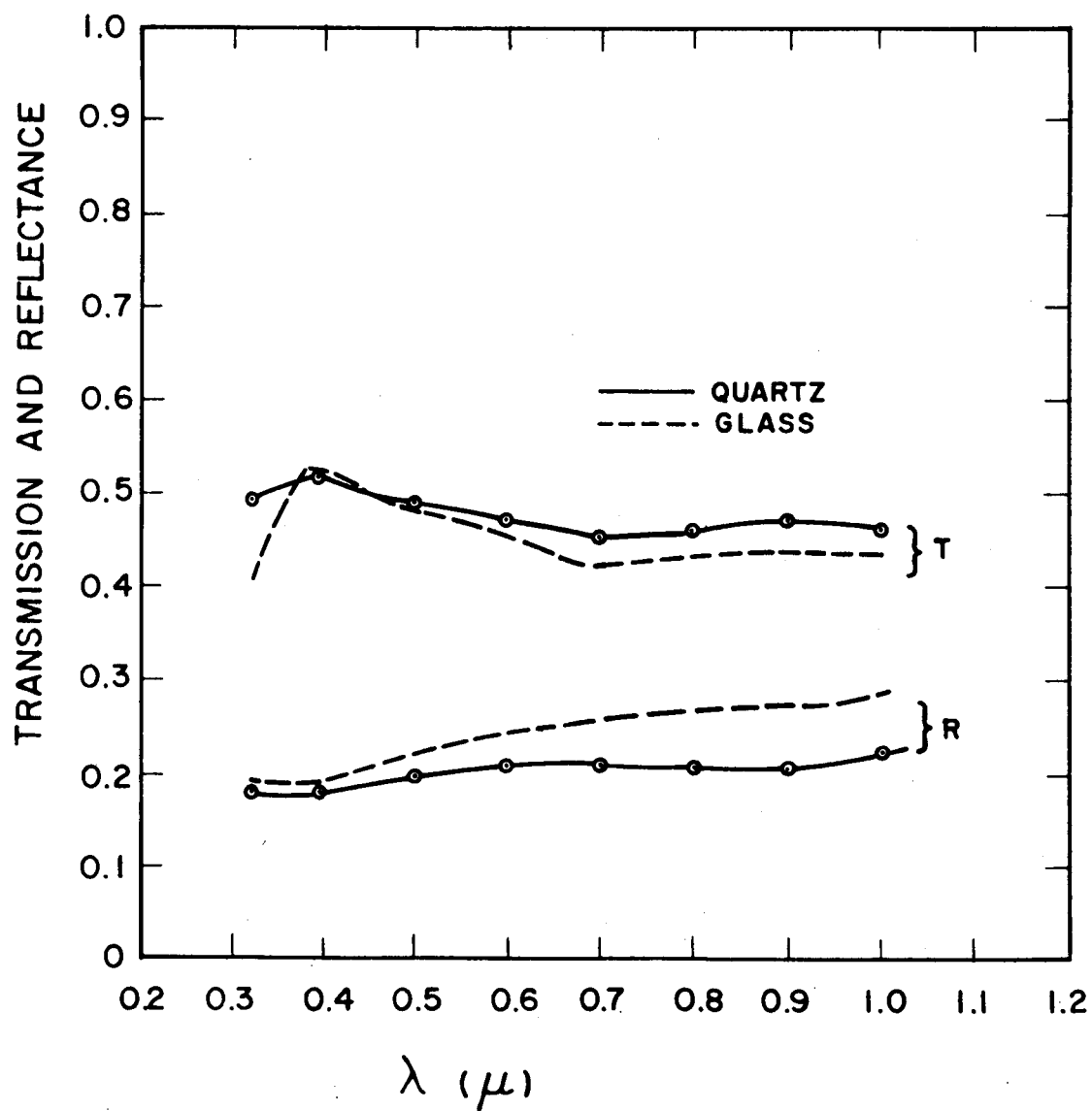
FIG. 3-8 BEAM SPLITTER TRANSMISSION REFLECTANCE AT 45°

The data from Table 3.3 can be used in Equation 3.2 to give the T_0o and T_{90}o transmission values shown in Fig. 3.9. As can be seen, the average ILS optical transmission is about 4%. Also, the apparent modulation of the light by virtue of the arm rotation is 2.4%.

3.2.3 Solar Virtual Image Optical System

The purpose of the solar virtual image optical system is to perform four spectral and one white light reflectance measurements on the solar-collector test samples. This section includes a general discussion of the optical system, alignment problems, system transmission, and the spectral and white light measurements.

3.2.3.1 SVI Optical System

Details of the SVI optical system can be seen in Fig. 3.2 and the photo (Fig. 3.10). All refracting elements of the SVI optical system are made of General Electric 151 fuzed quartz. This was done not only to simulate optical conditions for the satellite-borne instrument but also to be able to perform a near-ultraviolet spectral measurement. All reflecting elements in the SVI system are uncoated aluminum.

Solar radiation from the heliostat enters the reflectometer from the quartz window located in the top structural disk. This window is located in the same radial direction as the zero percent calibrate position (Section 3.2.4) so that the obscuration of the window by the arm presents no problems. The purpose of the window is, of course, to simulate the sealing window of the satellite-borne instrument with a sealed system (bearings). After passing through the quartz window the sunlight impinges on a spherical convex reflector (5 cm radius of curvature) which forms a virtual image of the sun. This virtual image is the light source of the SVI optical system. Light from the virtual image is reflected by two flat mirrors to the collimating lens. The purpose of the two mirrors is to obtain the proper sun-line-of-sight/optical axis angle and to be able to adjust
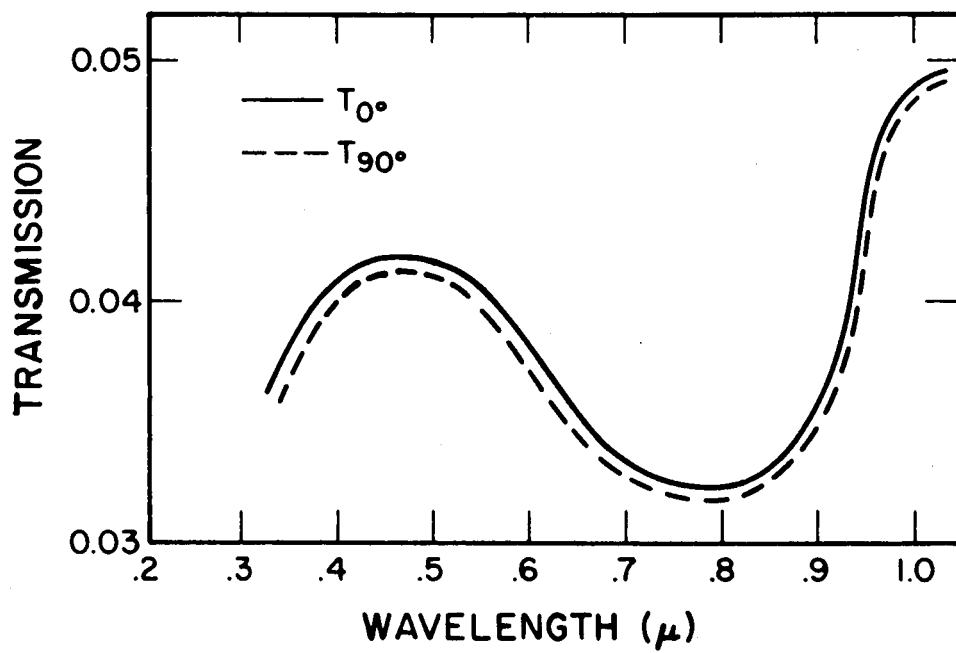
FIG. 3-9 ILS OPTICAL SYSTEM TRANSMISSION
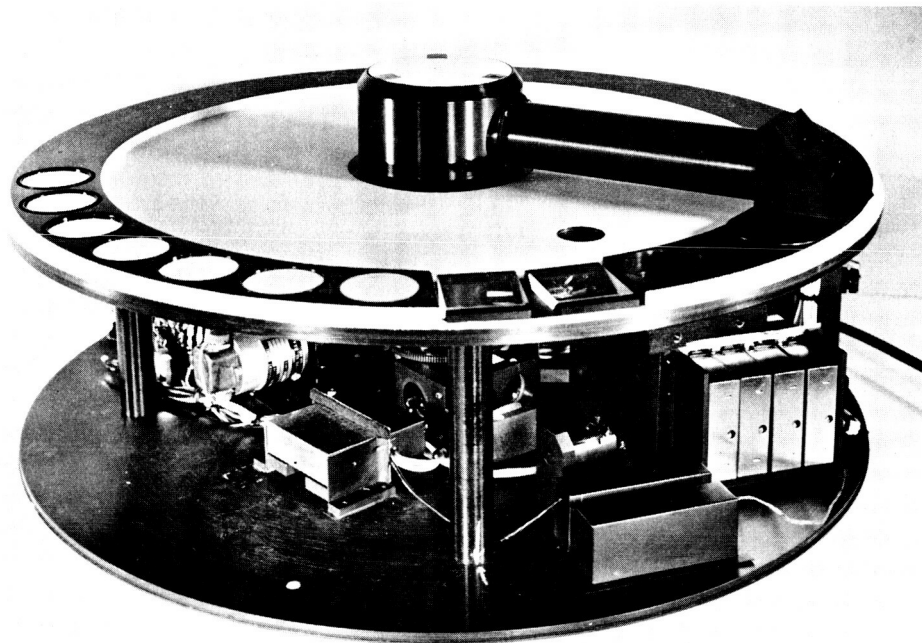
FIG. 3-10 REFLECTOMETER, SKIRT REMOVED

the spherical reflector/collimating lens distance. The angle of the spherical mirror is adjustable and the upper of the two mirrors is adjustable in angle and height. The lower flat mirror and collimating lens are fixed. The collimating lens (plano-convex) has a 17 cm focal length with the plano side toward the virtual image and a 2 cm clear aperture.

After traversing the collimating lens the light path is similar to (but opposite) that of the ILS optical system, i.e., beamsplitter, M_3, tilted window, M_4, M_5, sample, M_5, M_4, tilted window, M_3, and beamsplitter. Here, of course, the light is transmitted through the quartz beamsplitter and reflects off the glass beamsplitter. After reflection off the last beamsplitter the light enters the quartz dispersing prism. Upon entering the first face of the 60° dispersing prism the light goes to the second face. Here the light is divided and part of it is refracted at the second face and is dispersed into the spectrum for the four spectral measurements. The other part is reflected from the second face, passes out through the third face for the white light reflectance measurement. Light passing through the prism in this latter method undergoes no dispersion. A field lens focusses the white light energy on the detector in a similar manner to the ILS system. To gain some spectral resolution, use is made of the astigmatism produced by the spherical convex reflector forming the virtual solar image. An array of four, 4 x 4 mm PbS detectors complete the spectral portion of the SVI optical system. Two flat mirrors are used in the SVI system because of spatial restrictions in the reflec- tometer. One mirror is between the 60° prism and the white light field lens and the other is between the prism and the four spectral detectors.

3.2.3.2   SVI System Alignment

There are two major causes of the SVI optical system misalignment. One cause is solar orientation and the other is sample misalignment. The problem of solar orientation is related to

the problem of satellite attitude control and represents a major
design interface between the reflectometer instrument and the satellite
system (in particular the attitude control subsystem).

The position of the solar virtual image is
a function of the average angle of incidence of the sunlight on the
spherical reflector. The term average is used because of the spherical
reflecting surface. If the position of the solar virtual image is
shifted due to satellite misalignment, then a misalignment of the optical
system occurs. If the spin axis of the satellite is considered the roll
axis, then the optical axis of the SVI system between the spherical
reflector and the collimating lens may be chosen as the yaw axis. The
pitch axis is then orthogonal to the other two axes. Satellite mis-
alignment in the pitch axis is the most serious and only this will be
considered.

Figure 3.11 illustrates the geometry between
the impinging solar radiation, the spherical reflector, and the colli-
mating lens. The angle γ_o is the average or nominal angle of incidence
of solar radiation on the reflector. The angle β, defined by $\beta = \gamma - \gamma_o$,
represents satellite misalignment in the pitch axis resulting in the
optical system misalignment θ. The radius of curvature of the spherical
reflector is R and d is the distance between the point of reflection of
the average ray and the collimating lens.

From the law of sines the following expression
can be written

$$\frac{\sin (\gamma + \psi)}{R \cos \alpha + d + b} = \frac{\sin \theta}{R} \qquad (3.8)$$

However

$$\gamma + \psi = 180 - \gamma$$

$$(3.9)$$

and $\sin (\gamma + \psi) = \sin \gamma$

SUNLIGHT

COLLIMATING
LENS

SPHERICAL
REFLECTOR

YAW AXIS
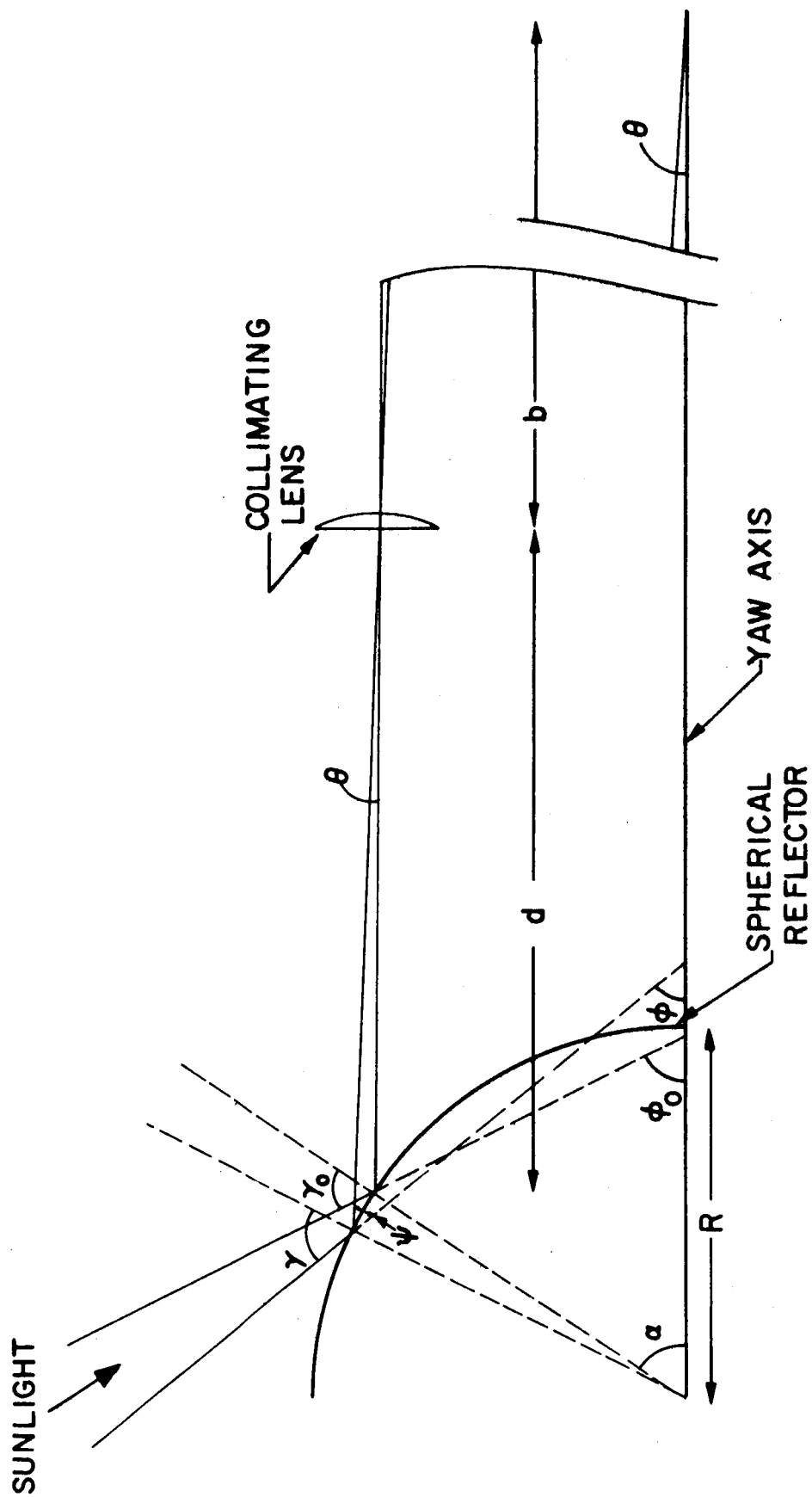
FIG. 3-11 SATELLITE ORIENTATION/SVI SYSTEM GEOMETRY-PITCH AXIS

Also,

$$b = \frac{R \sin \alpha}{\tan \theta} \qquad (3.10)$$

Substituting Equations 3.9 and 3.10 into 3.8 and rearranging terms we obtain

$$\sin \gamma = (d/R + \cos \alpha) \sin\theta + \sin \alpha \cos \theta \qquad (3.11)$$

This expression holds only when the angle θ is above the optical axis. When θ is below the optical axis Equation 3.11 becomes

$$\sin \gamma = (d/R - \cos \alpha) \sin\theta + \sin \alpha \cos \theta \qquad (3.12)$$

Equations 3.11 and 3.12 were solved numerically. Values for d/R, α, and θ were chosen and solved for γ. The term β was calculated for Equation 3.11 by means of

$$\phi = 180 + \theta - 2\gamma$$
$$\text{and} \quad \phi_o = 180 - 2\alpha$$
$$\text{and} \quad \beta = \phi_o - \phi = \gamma - \gamma_o$$

For Equation 3.12 the term β was calculated by means of

$$\phi = \theta + 2\gamma$$
$$\text{and} \quad \phi_o = 2\alpha$$
$$\text{and} \quad \beta = \phi_o - \phi = \gamma_o - \gamma$$

The results of these calculations are shown in Fig. 3.12 where the three main parameters affecting the SVI optical system misalignment are the angle α (which is related to the nominal sun line-of-sight/SVI optical axis angle), the ratio d/R and the
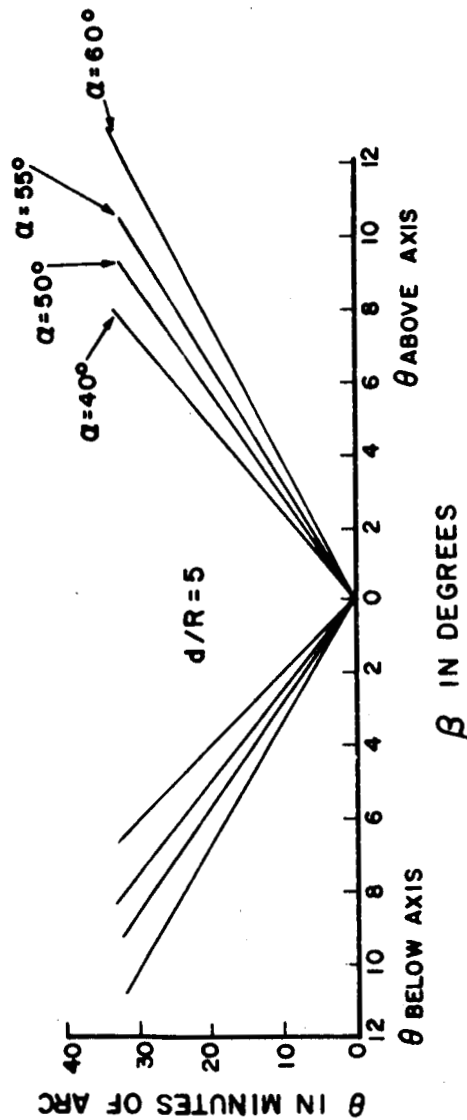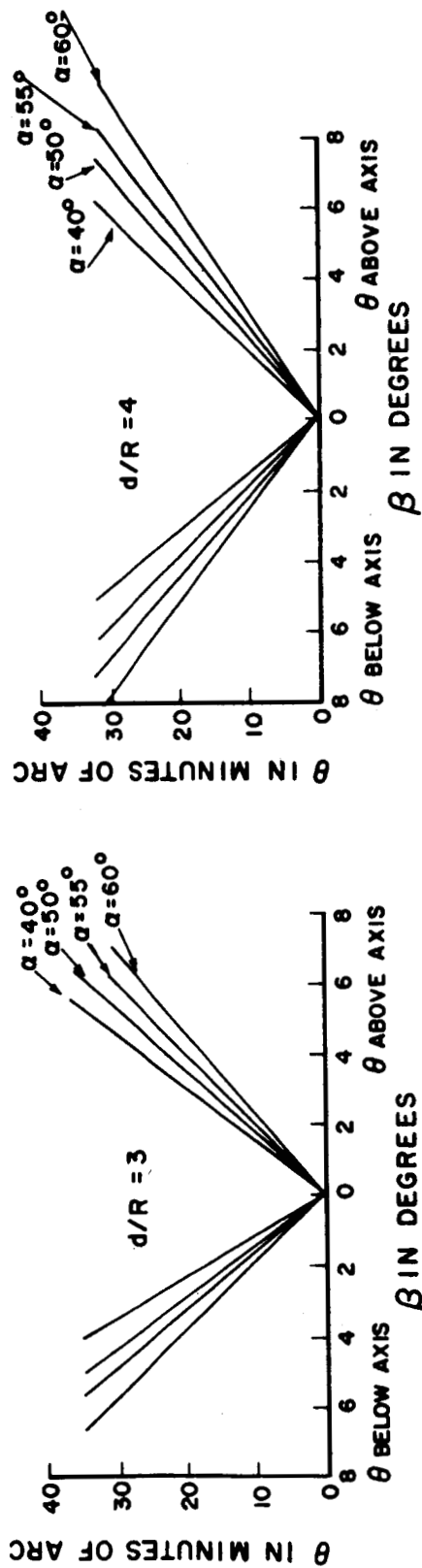
FIG. 3-12 SVI MISALIGNMENT DUE TO SATELLITE ATTITUDE

satellite solar orientation accuracy. From Fig. 3.12 it can be seen
that for a given satellite orientation accuracy the SVI optical system
misalignment can be minimized by increasing the angle α and the ratio
of d/R. As α increases the length of the astigmatic image (Section
3.2.3.4) increases and vignetting becomes a problem (assuming the
rotating arm cross section is constant). As the d/R ratio increases
the collected energy decreases by approximately the inverse square of
this ratio (assuming a constant aperture for the collimating lens).
These are the SVI optical system trade-offs with respect to satellite
attitude control. The demonstration model of the optical system has
a d/R ratio of about 4 and an α of about 40°. Under these conditions
a satellite attitude control accuracy of $\pm 4^\circ$ (which seems reasonable)
will result in a SVI optical system misalignment of 22 minutes of arc.
This misalignment can be accommodated by the SVI optical system white
light detector. The results of this misalignment on the spectral
measurements will be discussed in Section 3.2.3.4.

The other source of SVI optical system
misalignment is that due to the sample. With respect to the SVI white
light measurement the alignment considerations are very much the same
as with the ILS optical system. Here the critical factor is the size
(cross section) of the optical beam at the field lens since the field
lens images the sample on the detector. The average size of the beam
at the field lens is 0.6 cm. The clear aperture of the field lens is
2 cm (although it could be larger since it is further from the sample
than the field lens of the ICS system). Thus, the beam can be displaced
at the field lens ± 0.7 cm and still pass the clear aperture. The
distance from the field lens to the sample is 48 cm which represents a
sample misalignment of $\pm 0.8^\circ$ for the SVI white light measurement.

In the case of the spectral measurements a
sample misalignment will manifest itself in two ways. One is along or
parallel to the wavelength scale and the other is normal to this scale.
If any spectral resolution is to be maintained (via the astigmatic image)

it appears that very little can be done about the problem of sample misalignment manifesting itself parallel to the wavelength axis. This will result in a shift of the spectrum over the four detectors. This spectral shift could be measured (not a solution to the problem) by placing a beam splitter between the 60° prism and the white light field lens. This beamsplitter could reflect (or transmit) a portion of the beam energy to a pair of adjacent detectors which would measure the beam deflection (due to sample misalignment or attitude control) by a comparison of their resulting signals. This additional beamsplitter will lower the radiant energy falling on all the SVI optical system detectors but with a d/R ratio of 4 this is not expected to be serious.

A better solution to the sample and satellite attitude misalignment would be to modify the SVI optical system. This modification would consist of placing a short focal length field lens immediately adjacent to the last beamsplitter. This field lens would form a small image of the sample which would become the entrance slit for the spectrometer. The position of this image would be insensitive to sample misalignment and relatively insensitive to attitude misalignment. Also, the position of this image would be insensitive to any sample curvature. The light from this entrance slit image would be collimated by a lens and sent through the dispersing prism. Another lens would form an image of the entrance slit image at a distance compatible with the required spectral resolution, detector array size and angular spectral dispersion. This modification should solve the sample and satellite misalignment and sample curvature problems.

3.2.3.3 SVI Optical System Transmission

As with the ILS optical system, the SVI optical system transmission should be evaluated with respect to the light beam polarization components. This is especially true here since the reflections and refractions at the 60° prism could be particularly sensitive

to polarization. Table 3.4 traces the light path from the incoming
sunlight to the detector for the spectral measurements and Table 3.5
does the same for the SVI white light measurement. Of course, for the
satellite-borne instrument the two heliostat mirrors would not be needed.

Considering first the optical interfaces of
the spectral measuring system, interfaces 3, 7, 10, and 15 are the same
as T_A (Section 3.2.2.3) and have no polarization components. Interfaces
1, 2, 4, 5, 6, 9, 11, 12, 13, 14, 16, and 20 are the same as the R_{Bp}
and R_{Bs} terms of Section 3.2.2.3. Interfaces 8 and 17 are the same as
the T_{cp}, T_{cs}, and R_{cp}; R_{cs} (beamsplitter), respectively of Section 3.2.2.3.

Interfaces 18 and 19 can be calculated from
Fresnel's equations. The polarization reflection coefficients for the
reflection at interface 18 are

$$R_{18s} = \frac{\sin^2 (\phi - \phi')}{\sin^2 (\phi + \phi')} \qquad (3.13)$$

and

$$R_{18p} = \frac{\tan^2 (\phi - \phi')}{\tan^2 (\phi + \phi')}$$

where ϕ is the angle of incidence on interface 18 and ϕ' is the angle
of refraction ($\sin \phi' = \sin \phi / n$). The transmission of interface 18 is
then

$$T_{18s} = 1 - R_{18s} \qquad (3.14)$$

and

$$T_{18p} = 1 - R_{18p}$$

Interface	Optical Element	Type
1	Heliostat mirror	Reflection
2	Heliostat mirror	Reflection
3	Quartz window	Transmission
4	Spherical reflector	Reflection
5	Mirror	Reflection
6	Mirror	Reflection
7	Collimating lens	Transmission
8	Beamsplitter	Transmission
9	Mirror M_3 (Fig. 3.2)	Reflection
10	Quartz window	Transmission
11	Mirror M_4	Reflection
12	Mirror M_5	Reflection
Sample		
13	Mirror M_5	Reflection
14	Mirror M_4	Reflection
15	Quartz window	Transmission
16	Mirror M_3	Reflection
17	Beamsplitter	Reflection
18	Prism (60°) - first face	Transmission
19	Prism (60°) - second face	Transmission
20	Mirror (folding)	Reflection

TABLE 3.4   OPTICAL INTERFACES - SVI SYSTEM - SPECTRAL

Interface	Optical Element	Type
1	Heliostat mirror	Reflection
2	Heliostat mirror	Reflection
3	Quartz window	Transmission
4	Spherical reflector	Reflection
5	Mirror	Reflection
6	Mirror	Reflection
7	Collimating lens	Transmission
8	Beamsplitter	Transmission
9	Mirror M_3	Reflection
10	Quartz window	Transmission
11	Mirror M_4	Reflection
12	Mirror M_5	Reflection
Sample		
13	Mirror M_5	Reflection
14	Mirror M_4	Reflection
15	Quartz window	Transmission
16	Mirror M_3	Reflection
17	Beamsplitter	Reflection
18	Prism (60°) - first face	Transmission
19	Prism (60°) - second face	Reflection
20	Prism (60°) - third face	Transmission
21	Mirror (folding)	Reflection
22	Field lens	Transmission

TABLE 3.5   OPTICAL INTERFACES - SVI SYSTEM - WHITE LIGHT

In a similar manner the transmission of interface 19 can be written

$$T_{19s} = 1 - \frac{\sin^2 (\theta - \theta')}{\sin^2 (\theta + \theta')} \qquad\qquad (3.15)$$

$$T_{19p} = 1 - \frac{\tan^2 (\theta - \theta')}{\tan^2 (\theta + \theta')}$$

where $\theta = 60 - \phi'$ and $\sin \theta' = n \sin \theta$. Equations 3.14 and 3.15 were used to calculate the transmissions of interfaces 18 and 19 using $\phi = 28^\circ$. These transmission values are shown in Table 3.6.

	WAVELENGTH (μ)				
	0.35	0.40	0.50	0.70	1.00
T_{18s}	0.949	0.949	0.952	0.952	0.952
T_{18p}	0.975	0.975	0.975	0.977	0.977
T_{19s}	0.558	0.580	0.616	0.658	0.672
T_{19p}	0.843	0.864	0.891	0.918	0.925

TABLE 3.6   PRISM TRANSMISSION VALUES FOR
SPECTRAL MEASUREMENTS

The polarization transmission coefficients of the spectral SVI optical system for two different rotating arm positions (using the same V and 14 polarization directions as in Section 3.2.2.3) can now be written as:

$$T_{V\ 0^\circ} = T_A^4 \times T_{cs} \times R_{Bp}^{11} \times R_{Bs} \times R_{cs} \times T_{18s} \times T_{19s}$$

$$T_{V\ 90^\circ} = T_A^4 \times T_{cs} \times R_{Bp}^7 \times R_{Bs}^5 \times R_{cs} \times T_{18s} \times T_{19s} \qquad (3.16)$$

$$T_{H\ 0^\circ} = T_A^4 \times T_{cp} \times R_{Bs}^{11} \times R_{Bp} \times R_{cp} \times T_{18p} \times T_{19p}$$

$$T_{H\ 90^\circ} = T_A^4 \times T_{cp} \times R_{Bs}^7 \times R_{Bp}^5 \times R_{cp} \times T_{18p} \times T_{19p}$$

and

$$T_{0^\circ} = \frac{T_{V\ 0^\circ} + T_{H\ 0^\circ}}{2} \qquad (3.17)$$

$$T_{90^\circ} = \frac{T_{V\ 90^\circ} + T_{H\ 90^\circ}}{2}$$

Table 3.7 shows the results of Equations 3.16 and 3.17.

$\lambda\ (\mu)$	$T_{V\ 0^\circ}$	$T_{V\ 90^\circ}$	$T_{H\ 0^\circ}$	$T_{H\ 90^\circ}$	T_{0°	T_{90°
0.35	0.0110	0.0131	0.0250	0.0211	0.0180	0.0171
0.40	0.0122	0.0146	0.0282	0.0234	0.0202	0.0190
0.50	0.0123	0.0153	0.0296	0.0239	0.0210	0.0196
0.70	0.0076	0.0104	0.0222	0.0158	0.0149	0.0131
1.00	0.0175	0.0216	0.0390	0.0319	0.0283	0.0268

TABLE 3.7   SVI SPECTRAL MEASUREMENT
POLARIZATION AND TOTAL TRANSMISSION VALUES

Considering now the transmission of the SVI white light measuring portion of the optical system, the optical interfaces are the same as the spectral up to and including Interface 18 (Table 3.5). The reflection from Interface 19 is calculated from Fresnel's equations as is the transmission of Interface 20. Interfaces 21 and 22 have been described before. The polarization transmission coefficients of the white light SVI optical system for two different rotating arm positions can now be written as

$$T_{V\ 0^o} = T_A^5 \times T_{cs} \times R^{11}_{Bp} \times R_{Bs} \times R_{cs} \times T_{18s} \times R_{19s} \times T_{20s}$$

$$T_{V\ 90^o} = T_A^5 \times T_{cs} \times R^7_{Bp} \times R^5_{Bs} \times R_{cs} \times T_{18s} \times R_{19s} \times T_{20s} \qquad (3.18)$$

$$T_{H\ 0^o} = T_A^5 \times T_{cp} \times R^{11}_{Bs} \times R_{Bp} \times R_{cp} \times T_{18p} \times R_{19p} \times T_{20p}$$

$$T_{H\ 90^o} = T_A^5 \times 7_{cp} \times R^7_{Bs} \times R^5_{Bp} \times R_{cs} \times T_{18s} \times R_{19s} \times T_{20s}$$

Table 3.8 shows the results of Equations 3.17 and 3.18.

λ (μ)	$T_{V\ 0^o}$	$T_{V\ 90^o}$	$T_{H\ 0^o}$	$T_{H\ 90^o}$	$T_{\ 0^o}$	$T_{\ 90^o}$
0.35	0.0083	0.0098	0.0045	0.0038	0.0064	0.0068
0.40	0.0084	0.0101	0.0043	0.0036	0.0064	0.0069
0.50	0.0072	0.0091	0.0035	0.0029	0.0054	0.0060
0.70	0.0038	0.0050	0.0019	0.0014	0.0029	0.0032
1.00	0.0082	0.0100	0.0031	0.0025	0.0057	0.0068

TABLE 3.8   SVI WHITE LIGHT MEASUREMENT

POLARIZATION AND TOTAL TRANSMISSION VALUES

Figure 3.13 shows the total transmission of both the spectral and white light portions of the SVI optical for rotating arm positions of 0° and 90°. The spectral system transmission is purposely higher than the white light since this energy has to be shared by four detectors. The adjustment of the energy ratio to the two types of measurements is the entrance angle of incidence to the prism. The dip in the transmission curves at 0.80 μ is due to the aluminized mirrors. The drop-off of the spectral measurement transmission in the violet is due to the energy division action of the prism, i.e., the violet is reflected more than the near infrared. This also explains why the transmission rises so sharply in the near infrared for the spectral measurement transmission curve.

The apparent modulation of the light beam by the action of the rotating arm is 7 - 8%. This is greater than the apparent modulation in the ILS optical system because the light beam is more polarized (due to the greater number of mirrors) when it enters the rotating arm. The transmissions of both the spectral and white light optical systems are admittedly low. However, all optical elements are performing necessary functions in the simulation of the satellite-borne instrument optical system (with the exception of the heliostat mirrors).

3.2.3.4 Spectral Measurements

The results of contract number NAS 1-2880 indicated that the measurement of spectral reflectivity was desirable in the evaluation of solar-collector sample degradation in the space environment. The knowledge of spectral reflectance degradation is not only useful with respect to engineering and scientific data of sample performance but also yields clues as to the possible causes of degradation. Therefore, it was recommended in the above contract that coarse spectral measurements be performed with the solar collector test satellite.
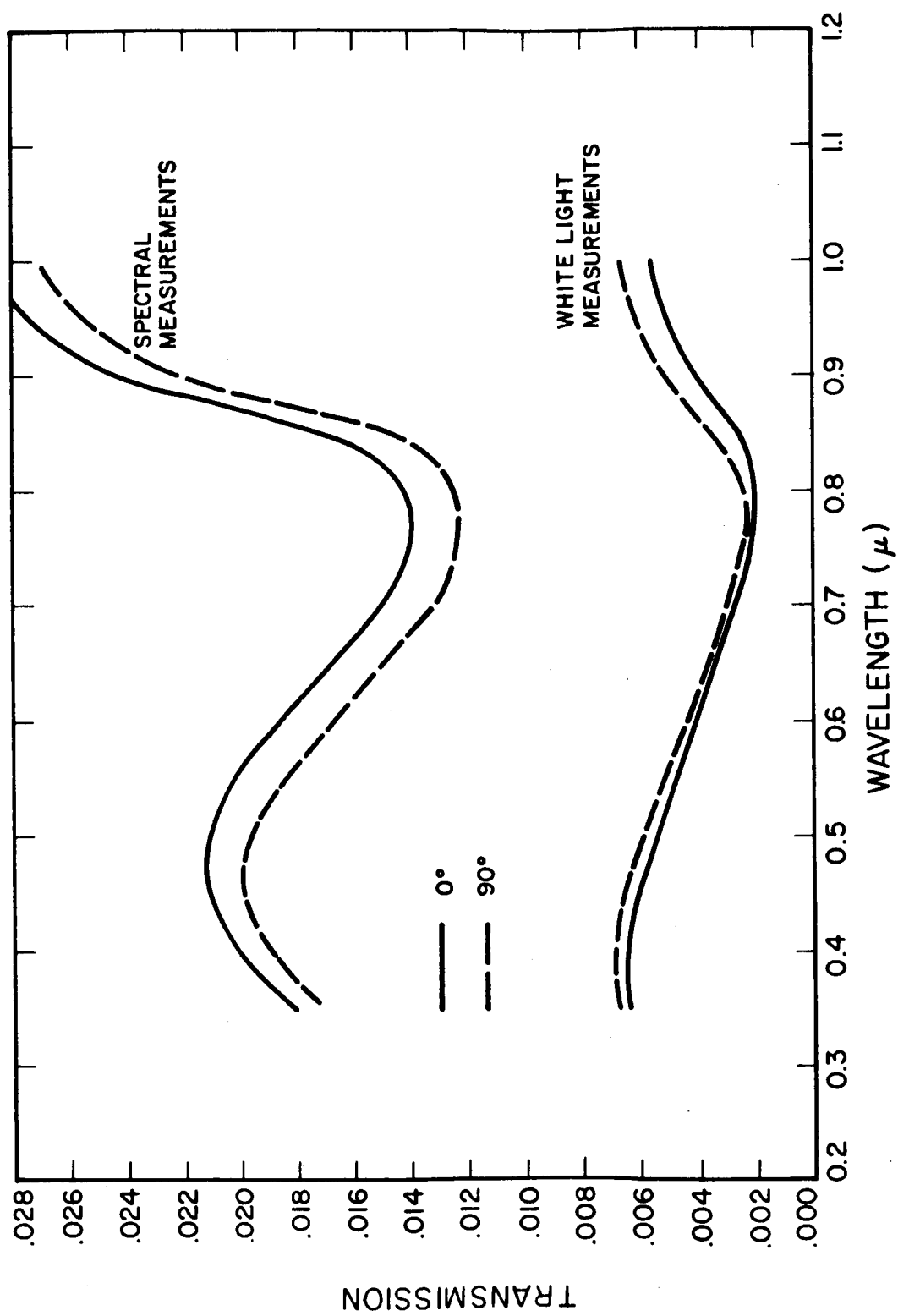
FIG. 3-13 SVI OPTICAL SYSTEM TRANSMISSION

In order to achieve meaningful spectral reflectance data some degree of spectral resolution must be realized. A degree of spectral resolution is achieved in the demonstration model optical system by focussing the astigmatic image formed by the spherical convex reflector and the collimating lens of the SVI optical system on the detector array. The light emanating from this combination of optical elements produces two mutually perpendicular astigmatic line images at different distances from the collimating lens.

For maximum spectral resolution the width of the astigmatic line should be a minimum. The width of the line is a function of the radius of curvature of the spherical reflector and the ratio of the image and object distances (magnification) of the collimating lens. The larger the radius of curvature of the spherical reflector, the wider the astigmatic line image will be. The image distance (optical path from the collimating lens to image) is rather large (due to the voyage up and back in the rotating arm) and fixed. Thus, the only control over image width is by means of the radius of curvature of the spherical reflector and the object distance which can be adjusted by changing the focal length of the collimating lens. To minimize the astigmatic image width the spherical reflector radius of curvature must be smaller and/or the collimating lens focal length longer. For a given collimating lens aperture, both these parameters will affect the light gathering ability of the SVI optical system by roughly their inverse square. Also, packaging considerations will limit the collimating lens focal length. Thus, a system trade-off must be achieved.

The length of the astigmatic image is a function of the angle between the sun-line-of-sight and the SVI system optical axis ($180 - \phi_o$, Fig. 3.11) and the angular aperture of the collimating lens. When $180 - \phi_o$ is zero the length of the image is the same as the width and there is no astigmatic line. As the angle $180 - \phi_o$ increases, astigmatism appears and the length of the image increases with very little increase in width.

With the demonstration model reflectometer the angle $180 - \phi_o$ is about 45°. Under these conditions the width of the line image is about 1 mm and the length is about 5 - 6 mm. The line image nearest the collimating lens is used since this is slightly smaller in width than the other image. The detector array consists of four 4 x 4 mm lead sulfide detectors immediately adjacent in a row. The detector size was chosen from image length, spectral dispersion, and signal-to-noise ratio considerations.

Since the width of the astigmatic image is somewhat fixed by the image distance and energy considerations (via spherical reflector radius of curvature and collimating lens focal length) the spectral resolution can only be increased by increasing the angular spectral dispersion of the quartz prism and/or the distance between the prism and the detectors. The angular dispersion is a function of the prism apex angle, the prism material, and the angle of incidence on the prism entrance face. An apex angle of 60° was chosen as a result of trade-off considerations of detector size (spectral resolution and prism/detector distance) and the division of energy between the spectral and white light measurements. The angle of incidence was chosen to be about 40° from the same considerations.

Figure 3.14 shows the angular dispersion curve for the 60° quartz prism with a 40° angle of incidence. The angles given in Fig. 3.14 are the angles of refraction of the light emerging from the second face of the prism. Curves are also given for 39° 50' and 40° 10' which would correspond to a $\pm 2^o$ satellite attitude control misalignment of the SVI system. It can be seen that this would result in a $\pm 0.02 \mu$ spectral shift at 0.4μ and a $\pm 0.16 \mu$ shift at 1.7μ. As will be seen shortly, this is comparable to the spectral resolution as determined by the astigmatic image size.

Figure 3.15 shows the solar spectrum outside the earth's atmosphere and at sea level with two air masses (this
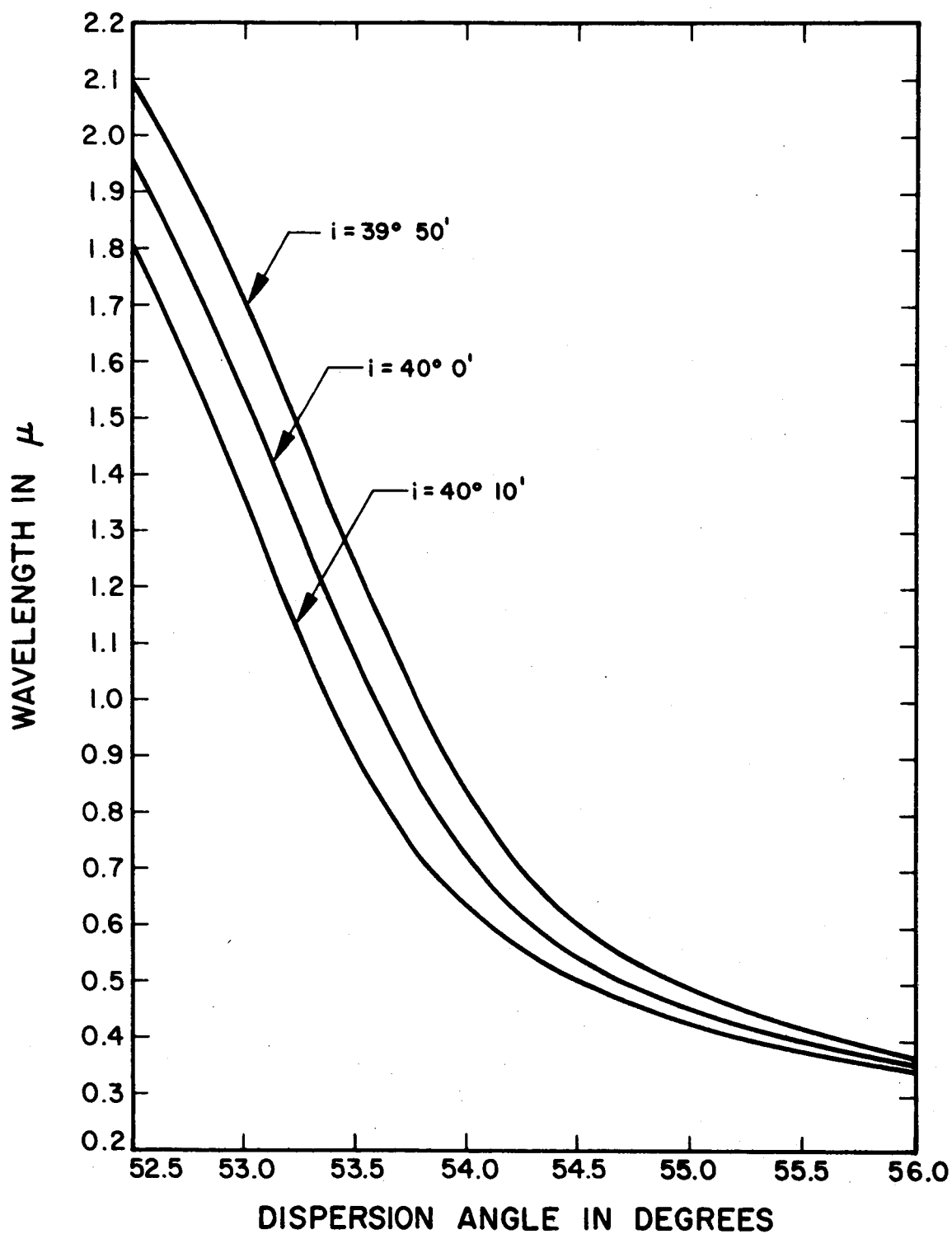
FIG. 3-14 ANGULAR DISPERSION OF 60° FUSED QUARTZ PRISM
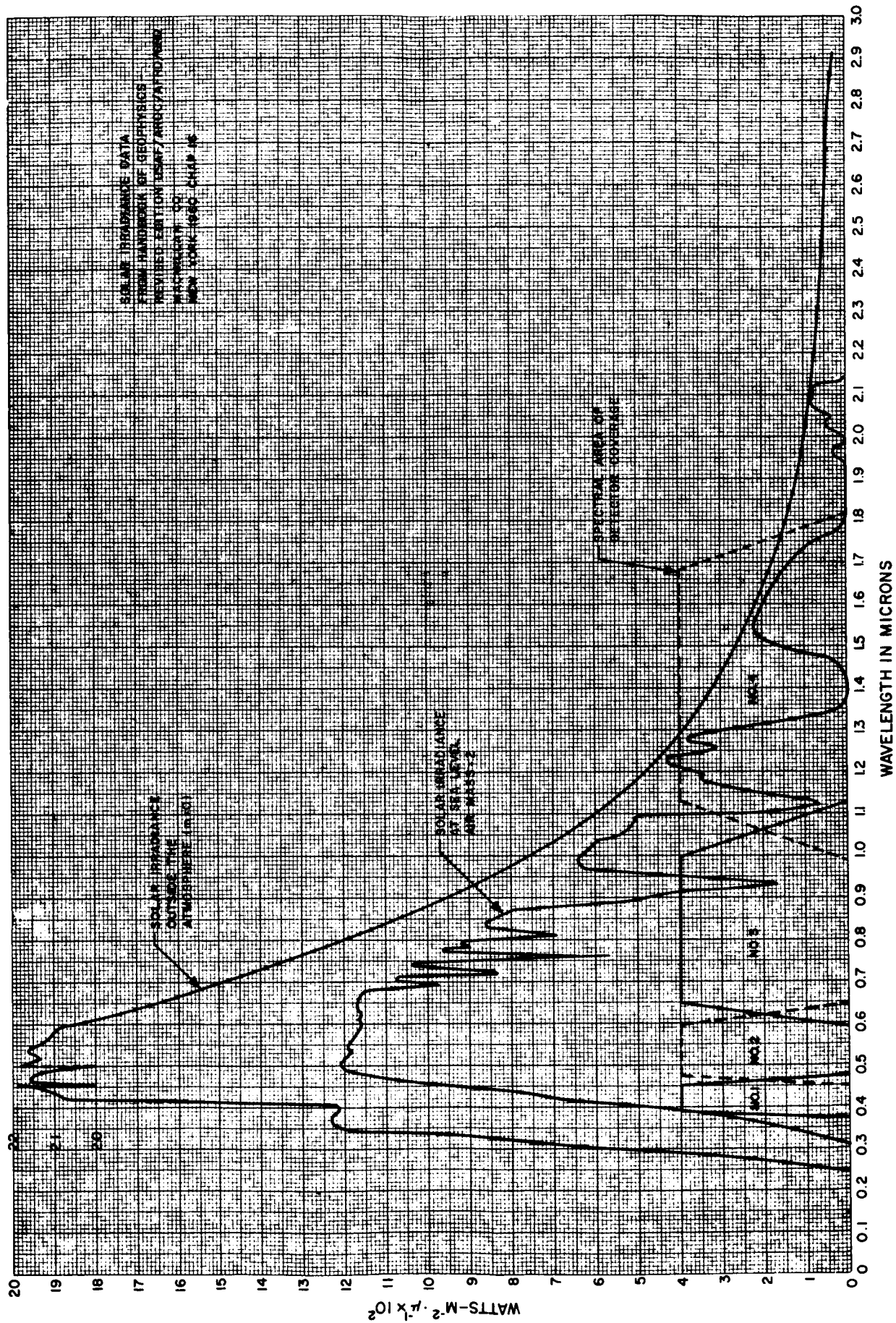
FIG. 3-15 SOLAR SPECTRAL IRRADIANCE AND DETECTOR SPECTRAL POSITION

corresponds to a 60° zenith angle). For the satellite-borne instrument it would be desirable to cover the spectral range from, say, 0.3 to 2.0 μ. However, the demonstration model reflectometer operates at sea level and the solar spectrum is cut down at either end of this spectral range by two air masses. Thus, the demonstration model covers the 0.38 to 1.75 μ spectral region. From Fig. 3.14 it can be seen that this represents a 2.9° angle (55.69° - 52.79° = 2.9°). If the total length of the detector array is 1.8 cm (this includes the interstices) then

$$\frac{1.8}{\tan 2.9°} = 35.5 \text{ cm}$$

and this is the distance between the prism and the detector array. Because of this distance it was necessary to use the optical path folding mirror.

Figure 3.15 also shows the spectral area of coverage of the detector array. The sloping lines between the areas of coverage represent spectral overlap due to the width of the astigmatic image. Because of the greater dispersion of quartz at lower wavelengths, the resolution is better in the blue than in the near infrared.

The resolution of the prism as determined by diffraction may be written (Ref. 8)

$$\delta \lambda = \frac{\lambda}{b} \times \frac{1}{dn/d\lambda}$$

where $\delta\lambda$ is the smallest spectral distance which can be resolved, b is the base of the prism (whose aperture is filled with light) and $dn/d\lambda$ is the dispersion of the quartz. The light beam, of course, does not fill the entire prism aperture (for misalignment purposes) but it would fill the aperture of a prism with a 0.5 cm base. Using this value for b, Table 3.9 shows the spectral resolution due to diffraction.

λ (μ)	$dn/d\lambda$ (μ-1)	$\delta\lambda$ (μ)
0.38	0.1359	0.00056
0.46	0.0601	0.00153
0.62	0.0345	0.00358
1.06	0.0119	0.01774
1.75	0.0130	0.0269

TABLE 3.9   PRISM SPECTRAL RESOLUTION DUE
TO DIFFRACTION

From Table 3.9 and Figure 3.15 we can conclude that the width of the astigmatic image limits the resolution of the SVI optical system and not diffraction.

A final consideration for the SVI optical system is the error incurred in the division of energy between the white light and spectral measurements due to a sample misalignment. Fresnel's equations were used in these calculations for the division of energy at the second prism face and the angle of incidence was varied about 40°. The reflection and transmission of all three prism faces were taken into account. Figure 3.16 shows the results for the white light detector at four wavelengths. The curves at the different wavelengths have about the same slopes. Figure 3.16 shows that a sample misalignment of $\pm$ 2° results in a 1.2% reflectance measurement error for the SVI white light. The same error holds for the SVI spectral reflectance measurements.

3.2.3.5 SVI White Light Measurement

Considerations for the SVI white light measurements are comparable to those of the ILS system with respect to misalignment causing vignetting at the field lens. Also, Section 3.2.3.4 contained some discussion of the SVI white light measurements where they interfaced with the spectral measurements.
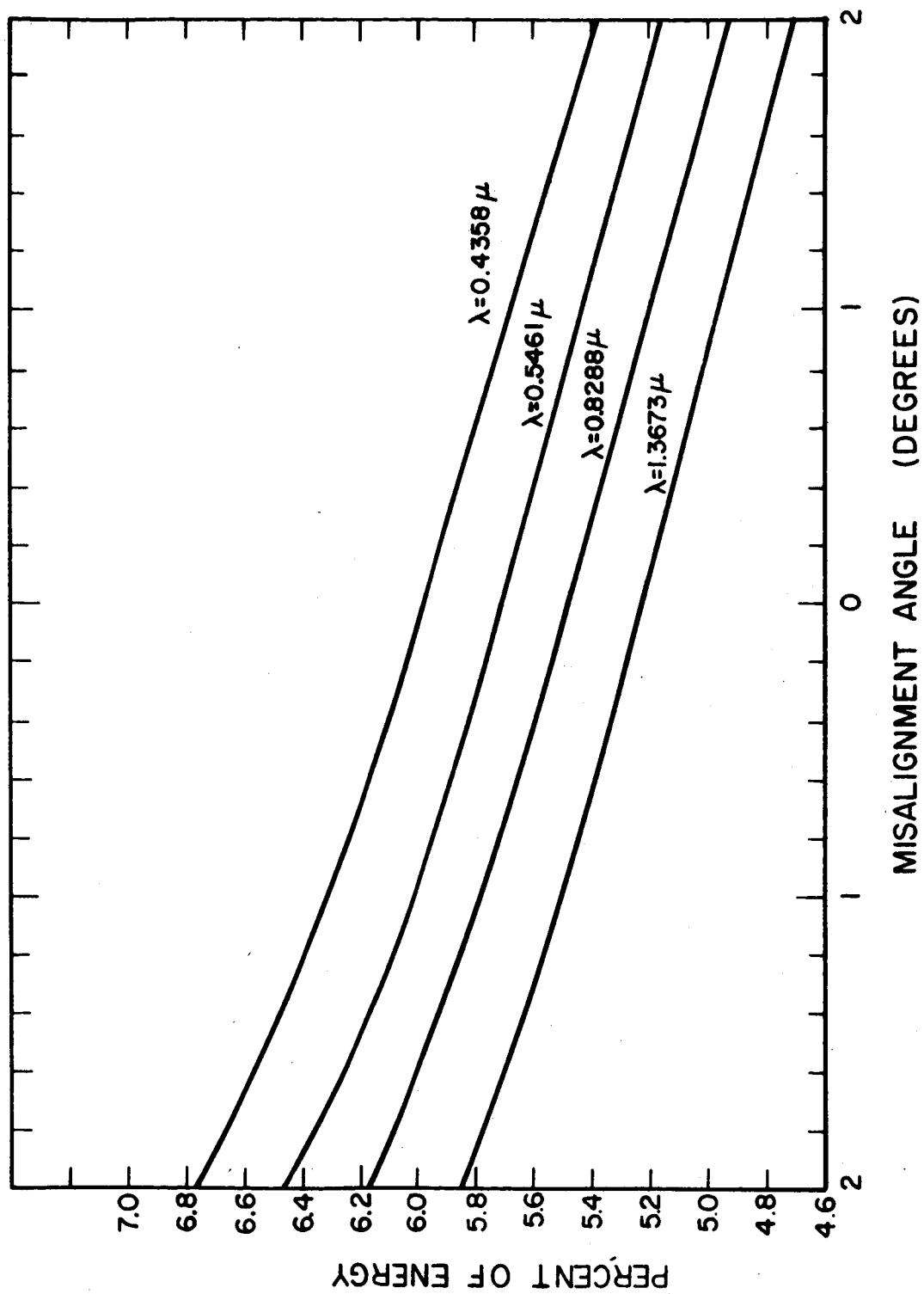
FIG. 3-16 PERCENT OF ENERGY REFLECTED TO WHITE LIGHT DETECTOR AS A FUNCTION OF SAMPLE MISALIGNMENT

3.2.4 Calibration

The demonstration model prototype reflectometer contains a calibrate prism located in one of the sample positions. The purpose of the calibrate prism is to be a standard to which all other samples are compared. The philosophy of this calibrate prism is that its reflectivity will not change (or change very little) upon exposure to the space environment. Actually, its exposure to the space environment (except vacuum) would be very low since the rest position of the reflectometer arm would be over the calibrate prism. Thus, the various elements of the optical system such as the interfaces (reflecting and transmitting), light source, detectors, and amplifiers need not be constant since all measurements are referenced to the calibrate prism.

The calibrate prism is made of fused quartz and has angles of 45°, 90°, and 45°. It is situated so that its hypotenuse face is normal to the incident light beam and thus is retrodirective in one dimension. It utilizes total internal reflection so that all radiation incident upon its hypotenuse is "reflected". Even the small amount reflected from its hypotenuse is reflected in the proper direction. The transmission of the fused quartz is expected to be quite constant in the space environment. Thus, the "reflectivity" of the prism is a function of the angle of incidence and its refractive index. In the direction normal to its retrodirectional properties, the prism acts as a mirror, i.e., angle of incidence equals the angle of "reflection". To minimize light losses, 90° angle has been fabricated as a "knife edge".

There are only two positions on the sample ring where the calibrate prism may be correctly mounted. These are at the rotating arm's azimuth positions of 0° and 180°. These azimuth positions occur when the axis of the rotating arm is parallel to the bisector between the ILS and SVI optical systems. The optical axes of these two optical systems are located at 2° from the bisector with the apex at the sample.

When the rotating arm is at the 0° and 180° azimuth position, the 2° angle is normal to the retrodirective axis of the calibrate prism and the light beam is returned to the proper detector in a manner similar to the samples. When the rotating arm azimuth position is at 90° and 270° the 2° angle is parallel to the retrodirective axis and the light beam returns back upon itself and will not reach the detector. This type of action causes the image of the filament (ILS) or virtual image (SVI) to scan across the field lenses as the arm passes across the calibrate prism. When the arm passes across a sample the image at the field lens is stationary. This scanning action does not present any problem since the image at the field lens is smaller than the field lens aperture and the resulting wave from the detector has a flat top.

Because of the low index of fused quartz the calibrate prism is totally internal reflecting between $\pm 1.35^o$ angle of incidence. This limit is at 2.0 μ and the lower the wavelength the greater the angular tolerance. Table 3.10 shows the plus and minus angle of incidence tolerance for the calibrate prism for 100% "reflection" for various wavelengths.

λ (μ)	Angle of Incidence
2.0	1.35^o
1.6	1.65^o
1.2	1.81^o
0.8	2.21^o
0.6	2.48^o
0.4	3.15^o
0.35	3.53^o

TABLE 3.10   ANGLE OF INCIDENCE VS WAVELENGTHS
FOR 100% CALIBRATE PRISM "REFLECTION"

An attempt was made to use another calibrate prism which was tilted slightly so as to give a 50% "reflectance" for calibration purposes. However, this prism was much too sensitive to alignment to be a reliable calibrate device. Finally, a black conical cavity is provided in a sample position for a 0% calibrate position.

3.2.5 Reflectance Samples

For economy reasons, only seven sample positions have been provided for on the demonstration model reflectometer. These seven samples cover a little less than 90° of rotating arm azimuth. Each sample is mounted in an adjustable cup. One sample is an optical aluminized (no overcoat) flat (glass substrate) which is used for evaluation and comparative purposes. The other six samples all have electroformed nickel substrates. Three of these samples have Al-SiO coatings. Two have Ag with Ucarsil (tarnish protection) overcoats and the last is coated with unprotected silver. The choice of sample coatings was arbitrary and merely attempted to present a variety of coatings (reflectances) to the reflectometer.

The optical flat sample is flat to 1/4 wave. The electroformed nickel substrate samples are convex with a focal length varying from -258 cm to -360 cm. These were measured by means of CW laser beam deflections across the sample face. This sample power has no apparent effect upon the quality of the image of the filament on the field lens of the ILS optical system.

3.3 Electronics

The electronic aspects of the demonstration model reflectometer consist of five subsystems. These are:

1. Detector/amplifier circuitry
2. Power distribution circuitry
3. Motor control electronics
4. Light source control electronics
5. Output selector electronics.

Also, the control panel contains various controls and condition indicators. With the exception of the detector/amplifier electronics the rest of the electronic subsystems are of secondary importance to the evaluation of the approach to the reflectometer demonstration model. These subsystems were included as a matter of convenience for the main instrument evaluation and to allow the demonstration model reflectometer to be a self contained unit (with the exception of the output display).

3.3.1 Detector/Amplifier Electronics

The detector amplifier electronics are shown in Fig. 3.17(a). The detectors are lead sulfide mounted on a quartz substrate and with a quartz protective window. The four spectral detectors are each 4 x 4 mm and the two white light detectors are each 2 x 2 mm. A resistance bridge circuit is employed where the detector is one resistance (variable according to the incident light) of the bridge. A second resistance is another lead sulfide detector which does not see any incident light. These two lead sulfide detectors are matched in resistance as closely as possible so their resistance vs temperature characteristics will track together. The two detectors are mounted back-to-back so as to be at the same ambient temperature. Black paper separates the two so the rear detector sees no light through the front detector. The 2 x 2 mm detectors have a nominal 850 K Ω resistance and the 4 x 4 mm detectors have a nominal 600 K Ω resistance. A trimpot is provided in series with one lead sulfide detector for matching purposes. The other two resistors are of the metallic film type whose temperature/resistance characteristics are very good. The metal film resistors are 500 K Ω with an accuracy of 1%. The detector bridge circuit board layout is shown in Fig. 3.17 (b). The detector is biased with 30 volts from a separate battery. Two batteries are used for all six detectors. One biases the four spectral detectors and the other biases the two white light detectors. A Philbrick P55 dc amplifier is used for each detector to amplify the signal to a 0 - 5 volt level.
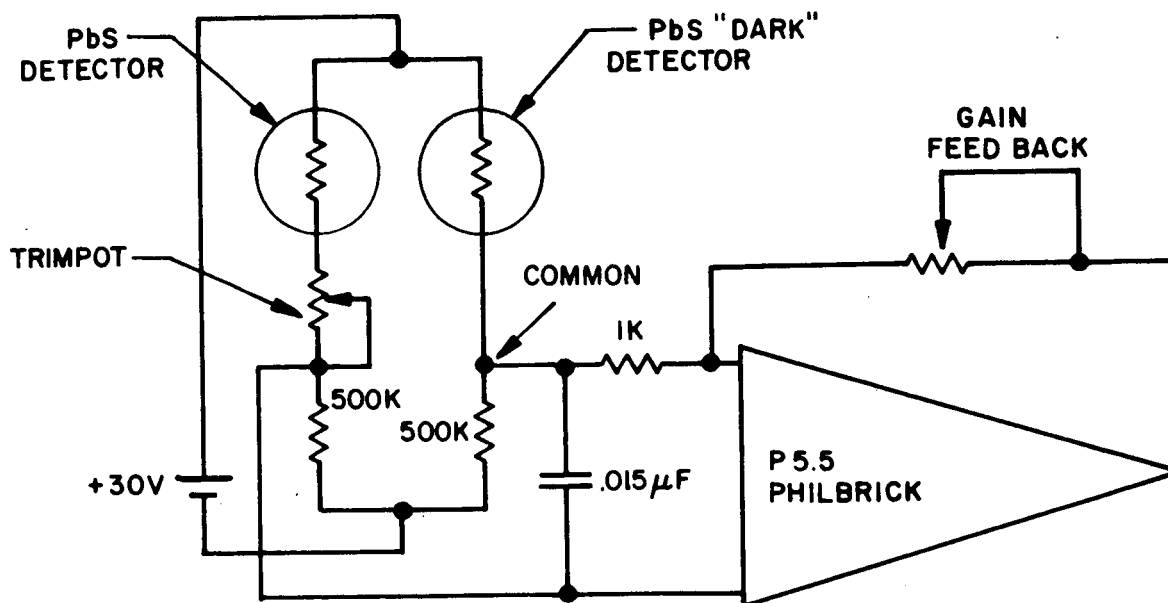
(a)   CIRCUIT DIAGRAM
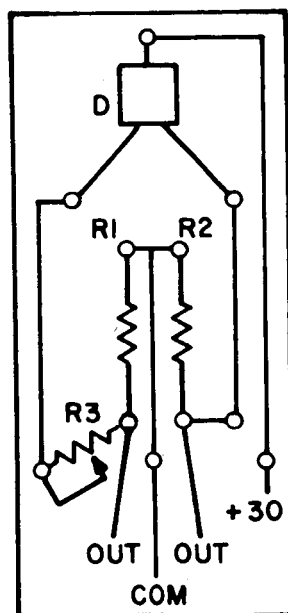
R1, R2 — METAL FILM 500K

R3 — TRIMPOT 100K

D — PbS DETECTORS, BACK TO BACK 2 x 2 mm

(b)   BRIDGE CIRCUIT BOARD LAYOUT

FIG. 3-17   DETECTOR/AMPLIFIER ELECTRONICS

3.3.2 Power Supply

Two 15 volt dc power supplies are mounted in the instrument to provide plus and minus 15 volts. The power supplies are not representative of the satellite-borne instrument and their output simulates the power subsystems of the satellite and allows the demonstration model reflectometer to be operated on single phase, 110 volt ac and draws a maximum of 40 watts. The dc power supplies provide power for the six amplifiers, the rotating arm assembly drive motor, the incandescent light source, and various control and indication circuitry.

3.3.3 Motor Control Electronics

The motor control electronics control the action of the motor which drives the rotating arm assembly. A three position switch is located in the front panel for motor control. One switch position will stop the arm as soon as it is actuated. When the automatic switch position is actuated the motor will continue to operate and will stop and come to rest over the calibrate position to simulate the desired arm action for the satellite-borne instrument. This operation is accomplished by a small magnet attached to the rotating arm assembly which actuates a reed switch to stop the motor at the proper positions.

3.3.4 ILS Control Electronics

The incandescent light source is operated from the power supply through a fixed resistance located on the rear control panel. Light source brightness is also adjustable by means of a variable resistance located on the rear control panel. The nominal voltage to the light source is 1.5 volts.

3.3.5 Output Detector Electronics

Since six detectors are used in the reflectometer, six output signals are present. These output signals can be sampled in sequence manually or automatically. The manual sampling has its own output jack and is controlled by the selector switch. Any detector may be sampled by means of the selector switch. The selector switch positions are:

1. ILS white light
2. SVI white light
3. SVI violet/ultraviolet
4. SVI blue/red
5. 0.6 - 1.0
6. Near infrared.

The automatic detector sampling is obtained from a second output jack. This operation switches from one detector to another every 360° rotation of the reflectometer arm. This switching is accomplished by a Ledex switch actuated by a reed switch and a magnet, the latter located on the rotating arm assembly. Six indicator lights on the control panel identify the particular detector being sampled. The indicator light numbers correspond to the selector switch numbers. The automatic detector switching may be by-passed by a miniature switch located on the back control panel.

3.3.6 Control Panel

The control panel is located in a cut-out in the reflectometer skirt. It accomodates the 110 volt ac power inlet cord and the fuse. It also provides mounting for the heliostat power connector. Three switches are mounted on the control panel. One is the main power and provides power to the power supplies and turns on the incandescent light. The second switch actuates the six amplifiers and the third controls the rotating arm motor (automatic and manual).

The detector indicator lights, manual selector switch, and two output
jacks are located on the control panel. The control panel is hinged
to permit access to the interior of the reflectometer.

3.4 Test Results

The demonstration model reflectometer has been tested and
the results are presented in this section. The ILS optical system has
performed in a very satisfactory manner. The test results of the
spectral portion of the SVI optical system leave something to be desired
mainly because of sample flatness. Problems of a general nature which
were also encountered are included.

3.4.1 ILS Optical System

Very little difficulty was encountered with the ILS
optical system. With a light source voltage of 1.5 volts an output
signal of 5 volts (after amplification) is easily achieved with an
amplifier gain of only 20. The noise level is much less than 1% of
full scale signal and the output waveform showed a good clean signal.
Also, under laboratory conditions, drift was less than 1% of 0%
calibrate for one revolution of the rotating arm (24 rpm). The ILS
could tolerate $\pm$ 1° sample misalignment and this figure could easily
be $\pm$ 2° with a different light source orientation, i.e., the ILS
signal levels are so high that the light source can be oriented to
give the smallest aspect ratio.

3.4.2 SVI Optical System

A great many operational problems were encountered
during the SVI optical system testing. The most serious were detector
drift (due to rapid fluctuation in the ambient because of local wind
and other thermal fluctuations) and the high ambient light level making
it difficult to make visual optical alignments. Tests were made under
these conditions but because the results were questionable (as a result
of the conditions) the tests were repeated in the laboratory using a
simulated sun. This simulated sun was a PEK X-35 Xenon short arc and

a lens giving a $1/2^{\circ}$ angular subtense to the light. A radiation thermocouple was used to measure the incident radiation of the simulated sun on the reflectometer. The thermocouple read 0.82 millivolts on the simulated sun whereas the real sun gave a reading of 7.4 millivolts. Thus, the simulated sun was roughly a factor of 10 in irradiance less than the real sun.

Table 3.11 shows the signal levels for the SVI optical system detectors. These were made on sample number 1 (the optical flat). Detector number 2 is the white light, number 3 is in the uv-blue, number 4 is in the green-red, number 5 is in the red $-1\,\mu$, and number 6 is in the $1 - 1.8\,\mu$ spectral region. The output signals for the simulated sun shows the reduced incident irradiance. In general, there appears to be sufficient radiant energy on the SVI system detectors to provide a 0 - 5 volt output with modest amplifier gain. The exception is the uv detector where the energy is quite low. However, the energy in this region of the spectrum is greatly attenuated by the atmosphere and Pasadena smog.

Detector	Output Signal (volts)		Amplifier Gain (approximate)
	Real Sun	Simulated Sun	
2	---	1.5	100
3	0.75	0.1	200
4	6	1.0	200
5	6	1.3	100
6	9	1.0	100

TABLE 3.11   SVI SYSTEM DETECTOR SIGNAL LEVELS

All signals appeared clean and noise was no problem. Output drift was checked in the laboratory with detector number 3 (highest gain) and using an arm rotation of 24 rpm an error in the reflectance measurement of 0.1% (worst case) would result. Thus, drift does not seem to be a problem with respect to reflectance measurement accuracy.

Alignment problems for the SVI optical system were pretty much as they were described in Section 3.2.3. However, sample curvature (Section 3.2.5) presents a serious problem in the case of the four spectral measurements. If the SVI optical system is focussed with the astigmatic line image on the detectors for the optical flat then this astigmatic image will be located in a different focal position when the arm is over the samples. This results in very poor spectral resolution. Also, because of sample curvature, the spectrum sweeps across the detectors in different directions depending upon the azimuth position of the sample. Sample curvature with respect to the SVI white light measurement behaves the same as the ILS system and presents no problem.

3.4.3 General Problems

The 100% calibrate prism is not located in the proper azimuth position. This error in positioning was not realized until it was too late to rectify it. However, its re-positioning is a relatively simple matter and it is understood that there are only two proper 100% calibrate azimuth positions.

Dectector drift does not seriously affect reflectance measurement accuracy but keeping the output signals within the 0 - 5 volt range is a problem. This could be overcome with chopping the light beam or ac coupling.

REFERENCES

Section 3

1. Index of Refraction of Fused Quartz Glass for Ultraviolet, Visible and Infrared Wavelengths, William S. Rodney and Robert J. Spindler, J. Opt. Soc. Am. 44, (1954)

2. W. Konig, Handbuch der Physik (Verlag Julius Springer, Berlin, 1928), Vol. 20, Chap 6

3. Hass and Waylonis; J. Opt. Soc. Am., 50, 1133 (TB15) (1960)

4. Schulz and Tangherlini; J. Opt. Soc. Am., 44, 362 (1954)

5. Schulz; J. Opt. Soc. Am., 44, 357 (1954)

6. Beattie; Physica, 23, 898 (1957)

7. G. Hass; J. Opt. Soc. Am., 45, 945 (1955)

8. "Fundamentals of Optics", Jenkins and White, Second Edition, McGraw-Hill Book Co. 1950, Page 292.

4. BEARING AND SEALS FOR OPERATION IN SPACE

A survey was made of available data relating to the design, operation, and reliability of moving parts in space. Particular attention was given to information pertaining to the problems encountered and overcome in the operation of seals.

To provide a conceptual design for the support and actuation of a reflectometer arm, the following systems for mounting the arm were investigated:

1. Partially rotating arm mounted on flexures
2. Partially rotating arm sealed with a bellows
3. Bearings suitably lubricated to operate in a hard vacuum
4. Pressurized bearings operating through seal

As a result of this investigation, it has been possible to arrive at a design configuration that offers maximum confidence based on present knowledge of bearings and seals.

4.1 Partially Rotating Arm Mounted on Flexures

If an arm is mounted on flexures, there are no bearings and no bearing problems. But a flexure-mounted arm is limited in rotation to approximately 60 degrees, depending upon the yield point of the material used. If a duplex flexure mount were employed the arm could be made to rotate through about 120 degrees. Were this system to be adopted, either the experimental satellite would have to be increased in size or the number of samples would have to be drastically reduced. Also, the drive mechanism for the flexure would have bearings (or seals) exposed to the space environment.

4.2 Partially Rotating Arm Sealed with a Bellows

When a partially rotating arm is hermetically sealed with a metallic bellows, it can rotate through only a few degrees. If an

elastomeric bellows made of material such as silicone rubber were sub-
stituted for the metallic unit, the angular rotation could be in-
creased to almost a full turn. Mechanically, this system would be
satisfactory because the bearings and drive would be sealed from the
affects of vacuum.

The use of polymeric elastomers is fraught with problems,
one of which is evaporation or sublimation in the hard vacuum of space
(Ref. 1). The Knudsen-Langmuir equation for the evaporation of
material in a vacuum is expressed as follows:

$$W = 5.83 \times 10^{-2} \; p \; \left(\frac{M}{T}\right)^{\frac{1}{2}}$$

where

$$p = (constant) \; e^{-\frac{B}{T}} \quad or \quad \log \; p = A - \frac{B}{T} \; ;$$

here,

        p = vapor pressure of material in torr

        W = rate of loss in $g - cm^{-2} \; sec^{-1}$

        M = molecular weight

        T = temperature, degrees Kelvin

        A, B = constants for each constituent of the material

Because polymeric materials are so complex generally, i.e.,
they are long chain compounds which can break down by depolymerization
or by heat into volatile fragments, it is difficult to compute the
losses by the above equation. However, outgassing rates for silicone
rubber are listed (Ref. 1). Material weight loss is shown to be quite
rapid at first, and then reaches a state of uniform weight loss which
is assumed to be constant over a long period of time. If silicone
rubber with the lowest rate of evaporation (1.6×10^{-5} $g-cm^{-2}$ hr^{-1})
is used, approximately 0.15 $g-cm^{-2}$ will have evaporated in one year.

If the wall thickness of the bellows were assumed to be 1 cm thick, and if the specific gravity of the material is assumed to be 1.25 (it can vary from about 1.13 - 1.45), then the weight loss would be $\frac{0.15}{1.25}$ x 100 = 12.4 percent.

The outgassed molecules of silicone rubber could, particularly during the initial heavy outgassing period, condense on the reflective samples of the experiment in spite of such a precautionary measure as a line-of-sight shutter.

Another problem associated with the use of elastomers in space is the affect of ultraviolet radiation, and neutron and gamma flux. Damage to elastomers by ultraviolet radiation is due to the ionization and excitation of the material's electrons. The changes are irreversible. Free radicals are formed; the material undergoes further polymerization and degrades by cleavage of carbon chains; and oxygen, hydrogen, and low molecular weight hydrocarbons are given off. These phenomena also occur with gamma-ray dosage (Ref. 2).

Because the elastomeric bellows would be continuously degrading in space by both evaporation and radiation, it is felt that this system is not attractive.

4.3 Bearings Suitably Lubricated to Operate in a Hard Vacuum

It is possible to operate ball bearings and gears successfully in space. Weinreb (Ref. 3) in his discussion of the successful operation of bearings and gears in the operation of the Tiros II meteorological satellite said that the radiometer system consisted of a series of mirrors, mounted on gears and eight ball bearings, driven by a motor of low power. The shaft speed of all bearings was 2750 rpm. "The radiometer operated successfully not only in vacuum-chamber testing but on the satellite, which has been (at the time of writing of Ref. 3) 2360 hours; no signs of deterioration had been observed at that time" (Ref. 2, p. 282).

The bearing requirements for the radiometer were the same as the requirements for the reflectometer arm: the alignment of

optical elements. Therefore, the bearings must not degrade and wear during the year of orbital flight. "Instrument ball bearings with conventional lubrication techniques were considered essential, since low power drain, long life, and reliability in space vehicles must be obtained" (Ref. 2).

The Tiros II radiometer bearings and gears were designed to be lubricated, but since no sealing was provided, lubricant evaporation was kept to a minimum. Since resistance to molecular flow for small orifices can be made relatively high, vapor pressure in the chamber behind the orifices also can be made high, thus reducing the vaporization of the lubricant in the chamber. A sintered porous nylon bushing, impregnated with a Mil-L-6085A diester oil, which has a vapor pressure of approximately 1×10^{-4} torr, serves as the lubricant reservoir. As the pressure outside the chamber drops below 1×10^{-2} torr, molecular lubricant flow begins to pass through the small annular clearance (0.0005-in.) around the shaft (See Fig. 4-1).

By means of the following equation, derived by Knudsen and others, it is possible to compute the escape rate of the oil molecules and to use this information for designing an unsealed, lubricated bearing system for the reflectometer arm.

$$ Q = \frac{4}{3} \sqrt{2\pi} \left[\frac{\left(R_2^2 - R_1^2\right)\left(R_2 - R_1\right)}{L} \right] \frac{1}{\sqrt{\rho_1}} (P_1 - P_2) $$

where

Q = flow rate of oil vapor

R_1, R_2 = inside and outside radii of annulus (Fig. 4-1)

L = length of annulus

ρ_1 = density of oil vapor at standard conditions

P_1 = pressure in housing

P_2 = ambient pressure

SINTERED NYLON
RESERVOIRS, VACUUM
IMPREGNATED WITH
DIESTER BASE OIL

ROTATING SHAFT
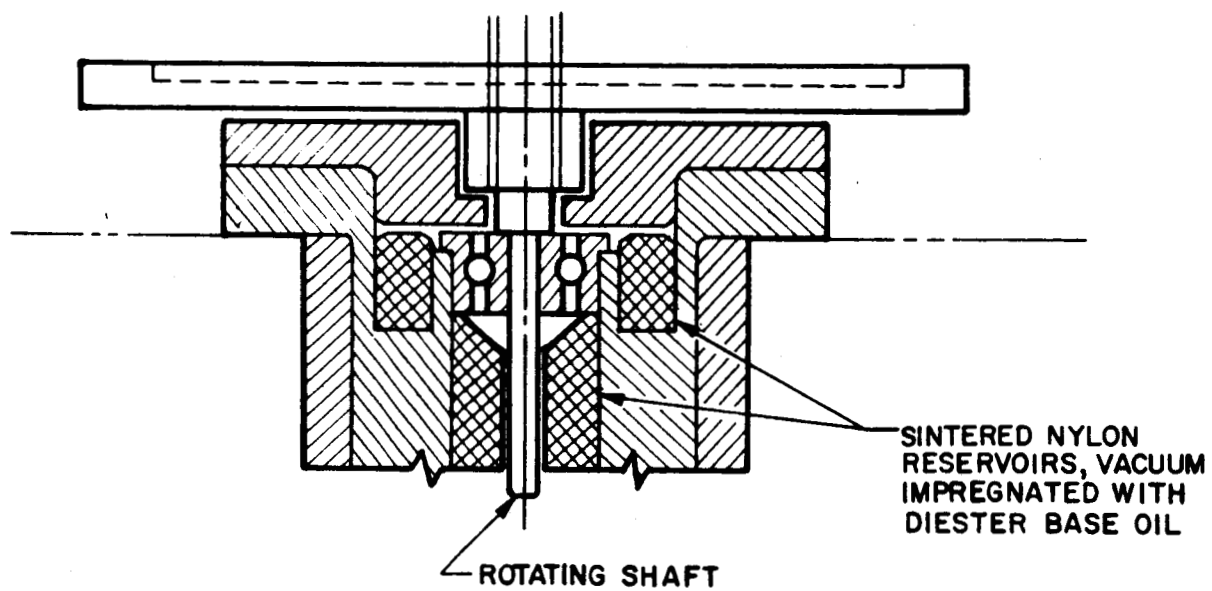
FIG. 4-1 RADIOMETER SPINDLE ASSEMBLY

In this design, the drive motor bearings and its gear box, the drive pinion on the motor shaft, the drive gear on the reflectometer arm, and the reflectometer arm bearings would have to operate at pressure p_1, which is very close to p_2, the ambient pressure; which, in turn, would range from 1×10^{-8} to 1×10^{-13} torr. Similarly, the motor brushes and commutator would have to operate under the same conditions. The Tiros II radiometer was equipped with an ac drive motor to eliminate brush problems. To use an ac motor in the satellite being designed would require the addition of a dc-to-ac inverter, an item of considerable mass.

Because the open lubricated bearing system has no seals, a considerable number of oil molecules will be expelled near the reflectivity samples; and, because of their large number, it is statistically probable that some of the particles could collect either on the samples or the reflectometer arm window and could interfere with the experiments.

4.4 Pressurized Bearings Operating Through a Seal

If a sealed system were used on the proposed reflectometer bearings and drive, the assembly would take the form of the unit shown in Fig. 4-2. In this design a sealed shell, pressurized by residual terrestrial atmosphere, contains the drive and bearing system. Without going into the seal problem for the moment, the unit is a tried and true conventional instrument-type mounting that has functioned successfully in many terrestrial units. The bearings are preloaded with a spring to eliminate play and to keep the reflectometer arm rotating in a true plane. Bearings and gears are prelubricated with grease so that no further source of lubricant is needed.

At the beginning of the orbital flight, the sealed drive shell will be at approximately 760 torr. As the flight progresses, some leaking will occur through the seal; and, until the end of the experiment, the pressure in the drive box should always be above ambient. Thus, it is necessary to provide a lubricant that will be effective even in a hard vacuum. The intent is to use methyl-phenyl-silicone oil with

BELLOWS

ROTATING HUB

WINDOW

REFLECTOR

STATIC SEAL

ROTATING SEAL

BEAM WIDTH

REFLECTOMETER
ARM

STATIC SEAL
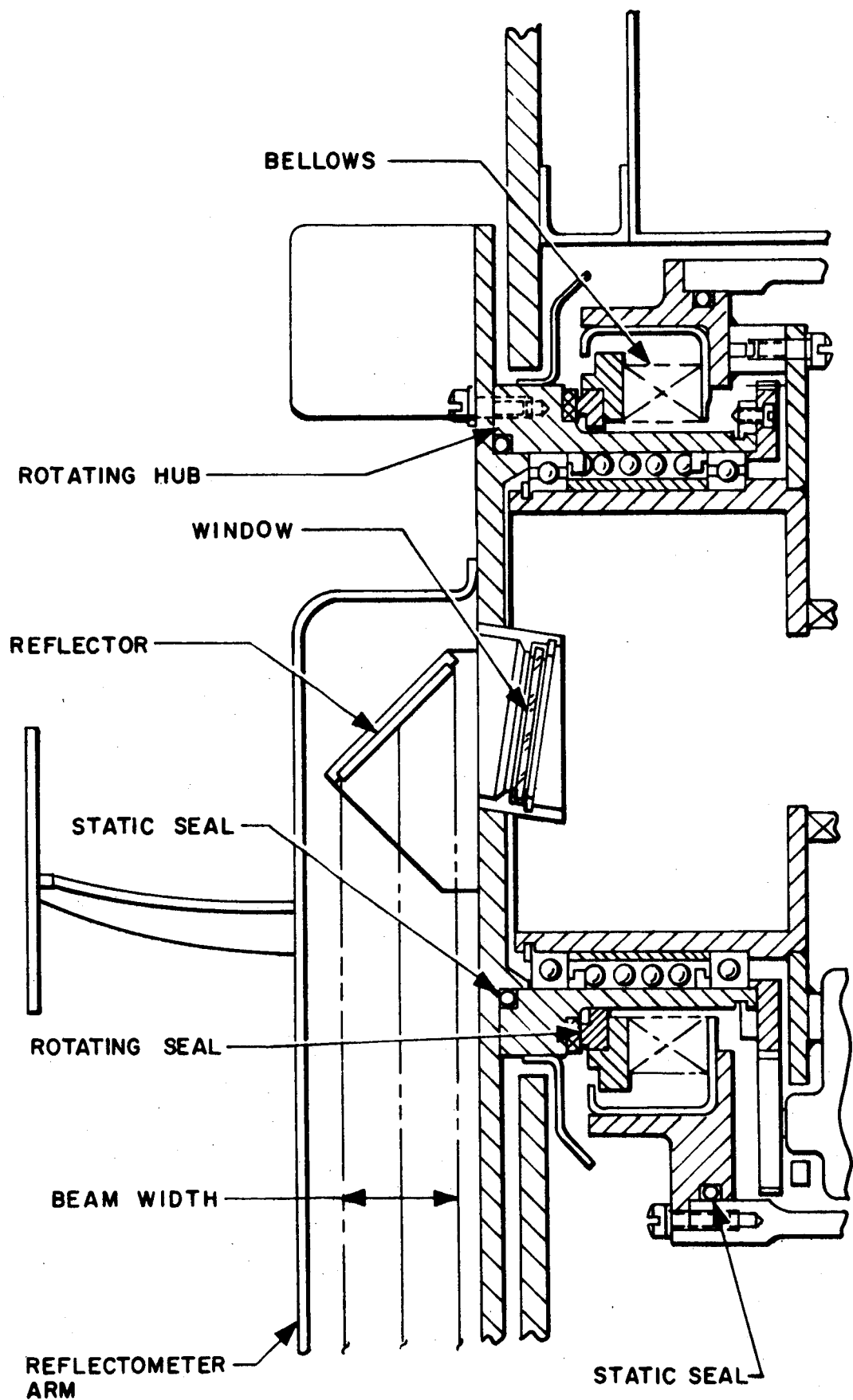
FIG. 4-2 SOLAR COLLECTOR DETAIL

dye thickener. This lubricant has been extensively tested at pressures ranging from 6 x 10^{-8} to 9 x 10^{-9} and temperatures varying from 160 to 225 degrees Fahrenheit on ball bearings that have run for over 13,000 hours (Ref. 4). "Furthermore, liquid lubricants which have high viscosity coupled with low vapor pressures can provide adequate lubrication for mechanical gear and bearing systems for use in space environment when completely sealed" (Ref. 5).

The seal is a standard metal bellows-type unit as shown in Fig. 4-3. The sealing surface of the sealing device would be coated with molybdenum disulfide (MoS_2) in a sodium silicate binder. The mating ring against which the MoS_2-coated surface would rub would be made of a sintered mixture of 80 percent silver and 20 percent MoS_2 (Ref. 6).

Heindl and Belanger, of Space Technology Laboratories, have performed a series of tests to evaluate MoS_2 sleeve bearings for space environment applications. During these tests shafts were oscillated in their respective bearings six times per minute for a total of more than 360,000 times in a vacuum of 1 x 10^{-7} torr at 80 degrees Fahrenheit. The shafts operated under a 15 psi radial load and were given a lengthy run-in under ambient conditions to assure proper mating. The results showed no seizure and a low friction coefficient throughout the life of the tests.

Even though these tests were conducted on a sleeve bearing, the rubbing action is almost identical with the sliding action of a sealing surface over its mating surface. Moreover, in the latter case, some of the molecules inside the sealed chamber would work their way out between the sealing surfaces. Some of these molecules would undoubtedly constitute lubricant vapors and would help to reduce the friction further. To prevent possible condensation of the organic molecules on the test specimens or reflectometer window; a shutter, mounted on the rotating shaft capsule, would block the line of sight of any outgassed molecule. Before committing the projected seal to

AMBIENT PRESSURE

MoS$_2$ COATING ON THIS SURFACE

METAL BELLOWS

HOUSING PRESSURE
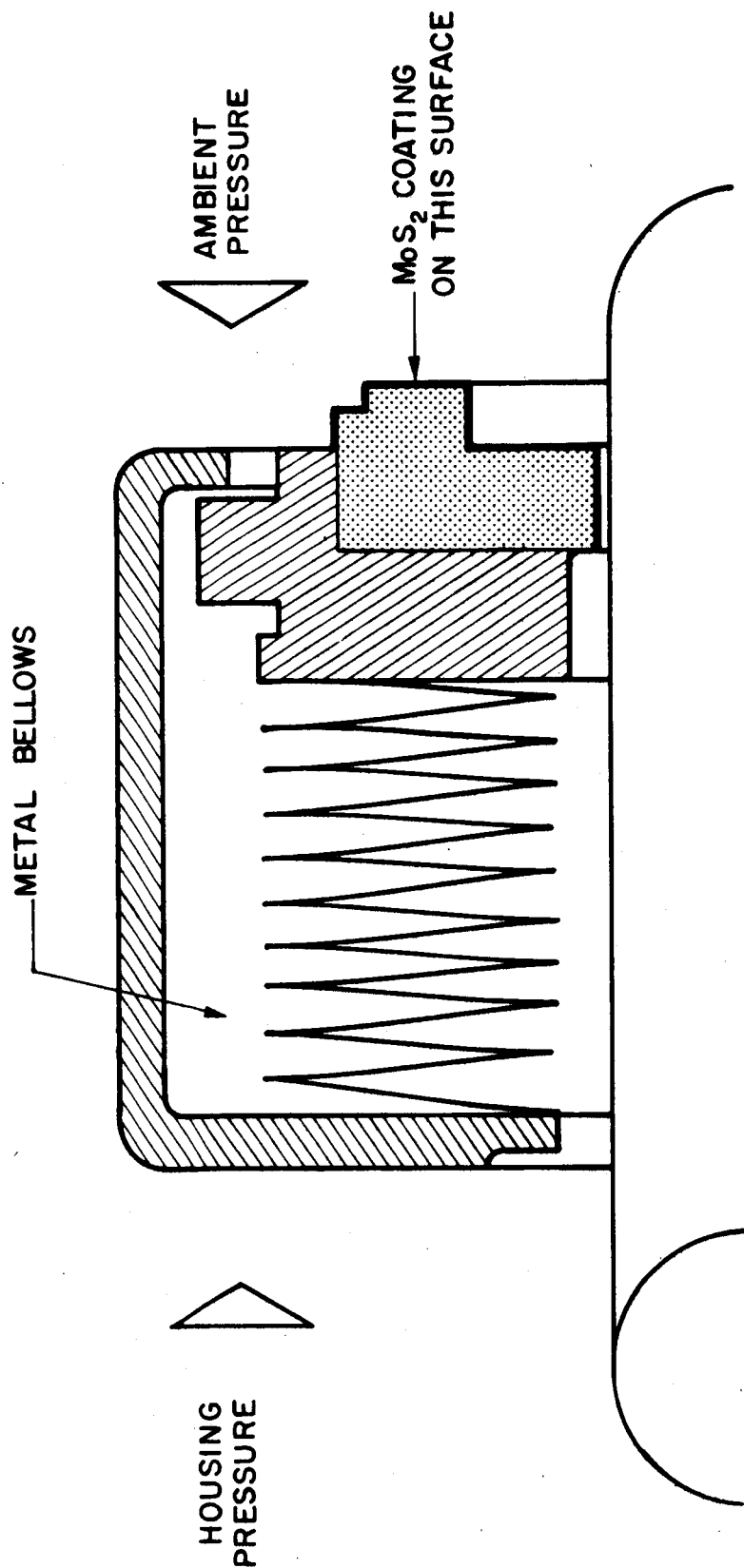
FIG. 4-3 METAL BELLOWS SHAFT SEAL

hardware, it would be advisable, as a further check, to run an evaluation test of the chosen materials under simulated conditions.

4.5 Conclusions

Of the four systems proposed for mounting the reflectometer arm, the sealed ball-bearing system seems to be the most feasible. The sealed system should be at least as reliable as the unsealed system and it has the added advantage of fewer contaminants being evaporated into adjacent areas within the satellite. The penalty of the added friction at the sealing surfaces is a low price to pay for the reduction in contaminants that would be generated by an open ball-bearing system.

Flexure-mounted and bellows-sealed partially rotating systems do not seem to possess the advantages of either a sealed or open ball-bearing continuously rotating system.

REFERENCES

SECTION 4

1. M. M. Fulk and K. S. Harr, "Sublimation of Organic Materials in Vacuum", Ball Brothers Research Corp., 9th National Vacuum Symposium, American Vacuum Society, pp. 324-33 (November 1962).

2. E. E. Bisson and W. J. Anderson, "Advanced Bearing Technology", NASA SP-38, Chap. 1, 2, 3, 6-9, Espc. Chap. 9 (1964).

3. M. B. Weinreb, "Results of Tiros II Ball Bearing Operation in Space", NASA 3-3568 (March 1961).

4. "Materials Research and Application Evaluation of Bearing Materials and Lubricants for Space Environment", Lockheed Missile and Space Company, A065438, AF 04(647)-787 (April 1963).

5. L. J. Bonis and G. S. Ansell, "Materials Selection and Development for Application in Inter-Planetary Vehicles", Ilikon Corp., 9th National Vacuum Symposium, American Vacuum Society, pp. 286-92 (November 1962).

6. J. C. Heindl and R. J. Belanger, "Space Friction Evaluation of Sintered MoS_2 Sleeve Bearings", Space Technology Laboratories, 10th National Vacuum Symposium, American Vacuum Society, pp. 27-31, (October 1963).

5. VALVING FOR ATTITUDE CONTROL

During the reporting period work was accomplished on the problem of valving for attitude control for the surface sample test satellite. This consisted of an analysis of the permissible valve leak rates, a study of the available components (some of which were used on the OSO), and a conceptual approach for the gas attitude control system. These are discussed in the following subsections.

5.1 Permissible Leak Rates

The feasibility of the gas control system depends on the ability of the nozzle control valves to hold the gas without excessive leakage. What is considered excessive depends on how much extra gas one is willing to allow in view of weight and bulk restrictions. It was shown in the Contract NAS 1-2880 Final Report that the gas pressure must be reduced to about 30 psi in order to obtain a manageable impulse when the nozzles are pulsed. The valves will therefore always work at a constant pressure and the leak rate will be independent of the amount of gas in the reservoir.

The control functions require about 250 g of N_2 for one year of operation. Allowing 10% for leakage, the leak rate is established at 25 g/yr. This is 8.3×10^{-7} g/sec or $\sim 6 \times 10^{-4}$ std cc/sec. Two valves will be needed, one for attitude control and one for spin up, so the permissible leak rate will be 3×10^{-4} std cc/sec for each valve.

The gas will be stored in the main reservoir at an initial pressure of 3000 psi and will be fed to an auxiliary reservoir at a constant 30 psi through a regulator. The permissible leak rate through the regulator will depend on the volume of the low pressure (LP) reservoir and the longest expected interval between control impulses.

Let P_o = Desired pressure in the LP reservoir

P = Actual pressure

t = Time between control impulses - seconds

m_o = Mass of N_2 corresponding to P_o - grams

f = Leak rate - g/sec.

Assume that f is independent of pressure so that in a time t the mass leak is f x t. Then the rise in pressure will be given by

$$\frac{P}{P_o} = \frac{m_o + ft}{m_o}$$

from which

$$f = \frac{m_o}{t} \left(\frac{P}{P_o} - 1\right)$$

Take the volume of the LP reservoir as 100 cc, then m_o = 0.28 g. The longest expected time between control pulses will be $\sim 10^5$ sec (about 1 day) and if we allow a 20% rise in pressure, P/P_o = 1.2. Therefore, $f = 0.28 \times 0.2 \times 10^{-5} = 5.6 \times 10^{-7}$ g/sec or 4×10^{-4} std cc/sec. This compares to the 3×10^{-4} std cc/sec leak rate for each valve for the assumed 10% leakage.

5.2   Available Components

There are two firms in the Los Angeles area who make valves and regulators meeting the leak rate specifications. One of these firms, Futurecraft Inc., furnished the valves and regulators for the OSO satellites. The permissible leak rate for the nozzle valves was 2.8×10^{-4} std cc/sec and, according to Ball Bros. Inc. who built the OSO, many valves were much better than that. The rated life of these valves is greater than 10^5 operations, whereas, we require only an estimated 12,000 to 15,000. The leak rate of the Futurecraft regulators is variable, diminishing as the downstream pressure increases.

The OSO regulators were connected to 10 cc low pressure reservoirs to which they delivered gas from the 3000 psi main storage.

The leakage increased the low pressure 10% in 1 hour, but only 20% in 100 hours, which corresponds to an average rate much less than the 20% per day for a 100 cc low pressure reservoir assumed in the NAS 1-2880 Final Report.

The other firm, Sterer Engineering and Mfg. Co., supplied the valves and regulators for Mariners B and C as well as for the Ranger and OSO vehicles. The leak rate for the nozzle control valves is 1.4×10^{-4}, and for the regulator, 5.6×10^{-4} std cc/sec. The latter figure is too high by about 40%, but could probably be reduced either by selection or by further design refinements. A simpler solution would be to increase the low pressure volume from 100 to 140 cc, which would increase the dimensions of the reservoir only 12%. The nozzle control valve opens in 12 ms, closes in 5 ms, and has a rated life of 10^6 operations.

5.3 Conceptual System

A conceptual sketch of the gas system is shown in Fig. 5-1. Attitude control signals are generated by the sun sensor whenever the sun's direction deviates from the sensor axis by some prescribed amount, as explained in the NAS 1-2880 Final Report, Section 4.3.4. The signal is amplified and shaped to produce a 0.1 sec pulse which drives the valve solenoid. Only one attitude control nozzle is shown because, as explained in the NAS 1-2880 Final Report, Sec. 4.3.8, there is no practical virtue in balanced torquing for this application. A lockout signal fed into the amplifier from the centrifugal switch prevents simultaneous operation of the attitude and spin control nozzles.

Spin rate is controlled by the centrifugal switch, which will close when ω (spin rate) drops to some preset limit. The spin control valve will then remain open until the switch contacts separate. There is only one spin nozzle for the same reason that there is only one attitude nozzle. However, although the attitude nozzle can be located anywhere so long as it is pointed along $\overline{\omega}$, the spin nozzle
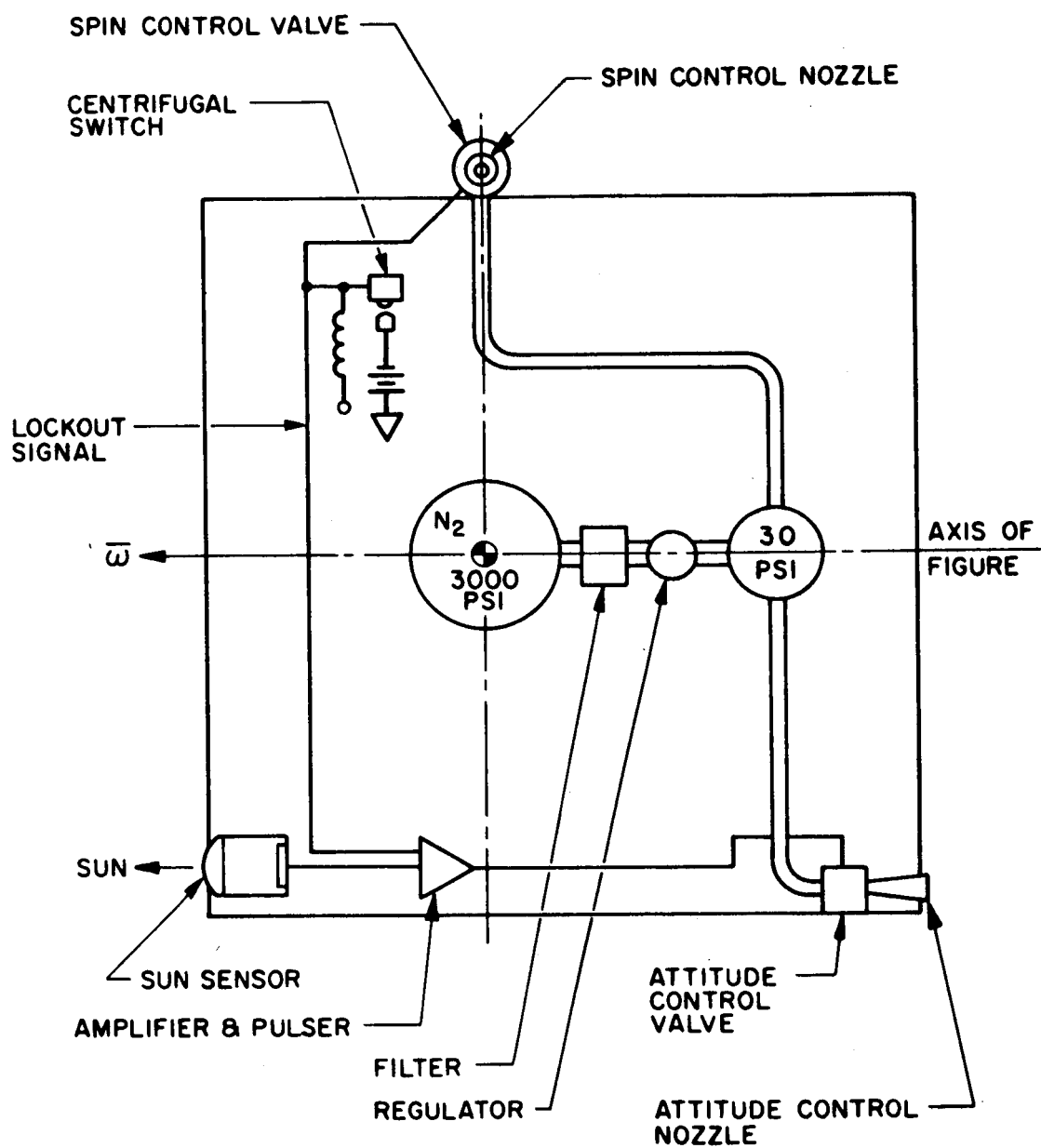
FIG. 5-1 GAS SYSTEM CONCEPT

must lie in a transverse plane through the center of mass. If it is not thus located it will cause a torque vector normal to $\bar{\omega}$ and the spin control operation will result also in an unwanted precession.

6.   PRELIMINARY RELIABILITY ANALYSIS OF SOLAR COLLECTOR TEST SATELLITE

This report contains the results of a preliminary reliability analysis of the Solar Collector Test Satellite (SCTS) described in EOS Final Report 4100 on contract NAS1-2880. Since the subject equipment is still at the breadboard stage of design, the reliability analysis performed at this time has been restricted to a concept and feasibility review.

A more sophisticated reliability analysis, involving determination of electrical and thermal stress levels for each individual part, precise failure rates for each part, failure modes and effects at the circuit segment level, etc., should be performed at a later stage in the overall program effort.

The rationale used in this reliability analysis is indicated by a description of the contents of subsequent subsections:

Section 6.1

Identify each building block, and element thereof, in the SCTS. Assess same in terms of failure rate per million hours.

Section 6.2

Identify the predominant failure modes for the items described in Section 6.1. Designate whether and to what extent each failure mode is critical in terms of experiment failure.

Section 6.3

By examining Sections 6.1 and 6.2 conjunctively, isolate the SCTS elements which: (1) have the highest probability of failure; (2) are most critical to the success of the experiment. Examine each of these potential trouble spots in terms of possible compensating provisions that would improve the overall SCTS reliability.

Section 6.4

Compute the SCTS's theoretical mean-time-to-failure (MTTF).

Section 6.5

Suggest a test plan for verifying the theoretical prediction of Section 6.4.

Section 6.6

Summarize the conclusions and recommendations which have evolved from the reliability analysis.

6.1 Gross Parts Count and Failure Rate Assessment

The following is a tabulation of the estimated failure rates for the various elements and building blocks comprising the Solar Collector Test Satellite:

6.1.1 Orientation Subsystem

Component	Failures per million hours
Solar Orientation Detector	1.0
Detector Amplifier	3.0
Trigger Former	1.0
Pulse Generator	2.0
Solenoid Driver	1.0
Attitude Jet Solenoid	15.0
Spin Control Solenoid	15.0
Centrifugal Switch	20.0
Reservoirs (2)	1.0 (each)
Filter	2.0
Nozzles (2)	1.0 (each)
Regulator	5.0

6.1.2 Power Subsystem

Component	Failures per million hours
Solar Panel	1.0
Clamp	0.5
Constant Current Charger	3.0
Battery	30.0
28V Regulator	2.0
13V Regulator	1.0

6.1.3 Environmental Measurement Instrumentation

Component	Failures per million hours
H. V. Power Supply	20.0
Stepping Motor	30.0
G. M. Tubes (3)	70.0 (each)
Scintillation Counter	30.0
Cadmium Sulfide Crystal (with broom magnet)	20.0
Dosimeter	15.0

6.1.4 Reflectometer Subsystem

Component	Failures per million hours
Tungsten Lamp	5.0
Detection Element (6)	3.0 (each)
Detector Bridge (6)	1.0 (each)
Detector Amplifiers (6)	4.0 (each)
Power Supply	10.0
Drive Motor	30.0
Rotary Switch	10.0
Bearings	5.0
Optical System (mirrors, collimating lenses, beam splitters, spherical convex reflector, prism, calibrate elements)	5.0

6.1.5 Thermal Measurement Instrumentation

Component	Failures per million hours
Temperature Sensors (30) (including voltage divider)	1.5 (each)

6.1.6 Telemetry Subsystem

Component	Failures per million hours
Command Reception, Command Decoding, and Power Programming Elements	40.0
Multiplexing Elements	30.0
Signal Amplifier	8.0
A-D Converter	15.0
Sync, Timing, Mixing, and Gating Elements	25.0
FM Transmitter	50.0
Bandpass Filter	2.0
Antenna	5.0

NOTE: Failure Rates assigned to the above circuit elements have been derived as follows:

1. Electronic part failure rates are as specified in the RADC Reliability Notebook.

2. Electromechanical and non-electronic part failure rates are based upon FARADA figures.

3. For those optical elements for which no failure rate data are currently available, EOS experience estimates have been used.

4. All electronic parts are presumed to be moderately stressed ($<50\%$) and used in an orbital environment.

6.2 Failure Modes and Effects

6.2.1 Orientation Subsystem

Predominant Failure Modes	Failure Effects
1. Attitude Control Valve does not activate properly.	Satellite may not be oriented to sun.
2. Spin Control Valve does not activate properly.	Satellite spinning cannot be stopped.
3. Centrifugal Switch does not function.	No maximum and minimum spin limitation.

6.2.2 Power Subsystem

Predominant Failure Modes	Failure Effects
1. Battery cells fail.	Insufficient power for experiment.
2. Battery charger fails.	Insufficient power for experiment.
3. Solar panel shorts out.	Battery cannot be charged.
4. Voltage regulators fail.	Regulated voltages not available for Command Channel and Instrument Subsystem.

6.2.3 Environment Measurement Instrumentation

Predominant Failure Modes	Failure Effects
1. G-M tubes fail.	Some radiation measurements not possible.
2. CdS Crystal fails.	Some radiation measurements not possible.
3. Sampling mechanism fails.	Cannot sample the individual environment detectors.
4. Power supply fails.	Cannot sample the individual environment detectors.

6.2.4 Reflectometer Subsystem

Predominant Failure Modes	Failure Effects
1. Tungsten lamp fails.	No artificial light source.
2. Reflectometer drive motor fails.	Specimens cannot be sampled.
3. Detector fails.	A portion of the spectrum or white light cannot be evaluated.
4. Power supply fails.	Specimens cannot be sampled.
5. Reflectometer structural failure.	Erratic or no data results.

6.2.5 Thermal Measurement Instrumentation

Predominant Failure Modes	Failure Effects
Temperature sensor fails.	The temperature of an individual specimen cannot be measured.

6.2.6 Telemetry Subsystem

Predominant Failure Modes	Failure Effects
1. Clock oscillator fails.	All timing ceases in subsystem and no data is transmitted.
2. Signal amplifier fails.	Low level data is not telemetered.
3. Telemetry transmitter fails.	Data is not telemetered or if failure is not catastrophic, transmission is at a reduced level or different frequency.
4. Command receiver and decoder fail.	Ground control of operating mode is lost.
5. Power programming fails.	Transmission of data and/or collection of data by instruments is no longer possible.

6.3 Reliability Optimization

Section 6.1 has defined the items which have the highest probability of failure; and Section 6.2, the effects of such failures. With this information, it is possible to identify the potential trouble spots in the SCTS and to recommend compensating provisions.

6.3.1 Orientation Subsystem

If the Orientation Subsystem fails and the satellite cannot be oriented to the sun, the experiment still can be performed by using the artificial light source (tungsten lamp). For this reason, and also because of the relatively low failure rates of the elements within this subsystem, no redundancy need be considered here. It is suggested, however, that the cycle-life capabilities of the two solenoid-activated valves and the centrifugal switch be substantiated for this SCTS application. This information can be based on: (1) vendor data; or (2) testing.

6.3.2 Power Subsystem

All elements within this block are critical to mission success. All electronic piece parts in this subsystem should be HI-REL types. A redundant string of solar cells, providing at least a trickle charge for the battery, should be included in case the master solar panel fails.

The most important hardware addition should be a redundant battery (5.5 pounds) which shares the work load. Either battery standing alone should be capable of providing the necessary power for the experiment.

As a modification to the present design, it is suggested that the output of the solar panel be provided with an additional parallel routing directly to the voltage regulators. This will allow the solar panels to feed the voltage regulators (for a limited period of time) in case of a battery failure.

6.3.3 Environment Measurement Instrumentation

This block is similar to the Orientation Subsystem in that a failure within it will not ruin the experiment. Its function is to provide information concerning the space environment. Each of the detection devices is paralleled; this will allow individual failures to occur without blacking-out the whole subsystem. Emphasis should, therefore, be placed on assuring the reliability of the rotary selector, its drive motor, and the associated power supply. No redundancy should be necessary in this subsystem.

6.3.4 Reflectometer Subsystem

This subsystem contains the instrumentation to be used for measuring specimen reflectivity. It is, therefore, critical to mission success. As previously mentioned, the tungsten lamp provides redundancy in case of a failure to the solar image optical system (and vice-versa). Each of the six reflectivity detectors has its own bridge and amplifier. Thus, individual detection system failures will not ruin the complete experiment.

The most sensitive portion of this subsystem is the reflectometer rotating arm and its associated drive assembly. It is suggested that a redundant motor be coupled to the drive motor shaft. The rotor of this second motor would ride along until such time as the first motor fails. If this occurred, switching circuitry would then activate the second motor to provide the necessary torque.

All electronic piece parts in this subsystem should be HI-REL types. All purchased assemblies should be rigorously tested for the intended application.

6.3.5 Thermal Measurement Instrumentation

The sensors proposed for this subsystem are inherently reliable because of their simplicity. Likewise, these items are connected in parallel, which means that failure of an individual sensor will prevent thermal measurements only on the specimen to which it is affixed. No redundancy is necessary in this subsystem.

6.3.6 Telemetry Subsystem

Because this subsystem is the final link in the chain of SCTS subsystems, and because all information passes through it, a failure in almost any of the principal modes mentioned in Section 6.2.6 will result in a mission failure. Even the Signal Amplifier is critical since the reflectometer outputs pass through it.

It is recommended that the following design concepts be employed in this subsystem.

1. HI-REL component types should be employed throughout.

2. The configuration for the Clock Oscillator should incorporate two cross-coupled solid-state multivibrators, each employing internal redundancy.

3. Hi-level data should not be attenuated and routed through the Signal Amplifier, but rather should be fed directly into the Analog-to-Digital Converter in parallel with the Signal Amplifier output.

4. The transmitted data format should be such that the most significant bit (MSB) of each word is transmitted first, so that failures in the A/D Converter and Parallel-to-Serial Converter will not necessarily destroy data transmission capability.

5. The telemetry Transmitter should be completely solid state with protection against power transients introduced by the power programming circuitry.

6. The Command Decoder/Receiver combination used in this subsystem should have a substantial history of failure-free field operation.

6.4 MTTF Computation

The mean-time-to-failure for the SCTS has been computed using the following assumptions:

1. The central core of the experiment can be reflected in a block diagram such as that shown in Fig. 6-1.

```
Command  →  ┌──────────┐   ┌────────┐   ┌──────────────┐   ┌────────────┐
            │ Command  │───│ Power  │───│ Reflectometer│───│ Telemetry  │──→ Data to
            │   S/S    │   │  S/S   │   │     S/S      │   │    S/S     │    Ground
            └──────────┘   └────────┘   └──────────────┘   └────────────┘
Command
Signal
```
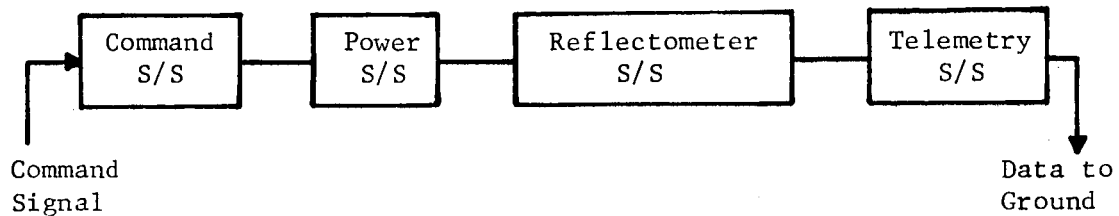
FIG. 6-1   EXPERIMENT MAJOR SUBSYSTEMS

2. The failure rate for the Orientation Subsystem has not been included in computing the SCTS mean-time-to-failure. This action is justified because: (1) the tungsten lamp will enable the experiment to be performed even if the Orientation Subsystem malfunctions; (2) most of the elements in the Orientation Subsystem have negligible "on" times.

3. The failure rate for the Environmental Subsystem has been omitted from the MTTF computation made herein because this subsystem can fail and the basic mission will still succeed.

4. The failure rate for the Thermal Measurement Instrumentation has also been purposely omitted from the MTTF computation which follows. The temperature sensors have inherently low failure rates, are connected in parallel, and can fail without destroying the basic experiment. Likewise, their contribution to the overall SCTS failure rate is negligible.

5. The complete set of specimen reflectivity measurements will be performed about 160 times during 1 year of orbital life. Each set of measurements will take 15 minutes to perform. The total reflectivity measurement "on" time will thus be about 40 hours.

7. The following redundant items are presumed to have been added to the SCTS (as recommended in Subsection 6.3):

   a. Additional string of solar cells

   b. A second battery.

   c. A second drive motor for the Reflectometer.

8. Electronic piece parts used in the Power Subsystem, the Reflectometer Subsystem, and the Telemetry Subsystem are presumed to be of HI-REL quality.

The remainder of this section is devoted to the presentation of MTTF computations used in this analysis. In these computations, the formula

$$R = 2e^{-xt} - e^{-2xt}$$

has been used to determine the failure rate of the redundant components.

MTTF COMPUTATION

BASIC EQUATION

$$R_{SCTS} = e^{-(x_C t_C + x_P t_P + x_R t_R + x_T t_T)}$$

where:

R_{SCTS} = the probability that the Solar Collector Test Satellite will operate successfully for one year

$x_C t_C$ = Command Subsystem failure rate x operating time

$x_P t_P$ = Power Subsystem failure rate x operating time

$x_R t_R$ = Reflectometer Subsystem failure rate x operating time

$x_T t_T$ = Telemetry Subsystem failure rate x operating time

6. The time factors (t) used in the MTTF computation are as
   follows:

$$t = 8760 \text{ hours}$$
(1-year mission)

$$\left\{ \begin{array}{l} \text{Power Subsystem} \\ \text{Antenna} \\ \text{Bandpass Filter} \\ \text{Command Receiver} \\ \text{Command Decoder} \end{array} \right.$$

$$t = 450 \text{ hours}$$
(reflectivity measure-
ment "on" time plus
tracking "on" time x 10

Telemetry Subsystem (ex-
cluding the four elements
listed on the previous
page)

$$t = 400 \text{ hours}$$
(reflectivity measure-
ment "on" time x 10)

Reflectometer Subsystem

NOTES: (a) A multiplier of (10) has been applied in determining two
of the time factors. The result is to increase (by an
order of magnitude) the "on" time reflected for the ele-
ments involved. This is to allow for: (1) the degrading
effect resulting from switching the items on and off a
total of 160 times; and (2) the fact that the items must
be continually prepared for an "on" command during the
1-year mission.

(b) In assigning these time factors, it was recognized that
some elements within the various subsystems were operative
for a greater or lesser period of time than has been as-
signed to the subsystem as a whole. In general, however,
errors of this type are not appreciable and tend to offset
each other. In all instances, the tendency has been to
be conservative in this MTTF computation.

COMMAND SUBSYSTEM

Calculating $x_C t_C$:

$$x_C t_C = (x_{\text{command receiver and decoder}})\ (8760) + (x_{\text{other command elements}})\ (450)$$

$$x_C t_C = (35 \times 10^{-6})\ (8760) + (5 \times 10^{-6})\ (450)$$

$$x_C t_C = 0.3087$$

POWER SUBSYSTEM

Calculating $x_P t_P$:

$$x_P t_P = (x_P)\ (8760)$$

From Section 6.1

$$x_P = \underset{\substack{\text{redundant} \\ \text{string of} \\ \text{solar cells}}}{0.1} + 0.5 + 3.0 + \underset{\substack{\text{redundant} \\ \text{batteries}}}{6.3} + 2.0 + 1.0 = 12.9$$

$$x_P t_P = (12.9 \times 10^{-6})\ (8760) = 0.1130$$

REFLECTOMETER SUBSYSTEM

Calculating $x_R t_R$:

$$x_R t_R = (x_R)\ (400)$$

From Section 6.1

$$x_R = 5.0 + 18.0 + 6.0 + 24.0 + 10.0 + \underset{\substack{\text{redundant} \\ \text{drive motor}}}{3.5} + 10.0 + 5.0 + 5.0 = 86.5$$

$$x_R t_R = (86.5 \times 10^{-6})\ (400) = 0.0346$$

TELEMETRY SUBSYSTEM

$$\text{Calculating } x_T t_T:$$

$$x_T t_T = (x_{\text{antenna and B.P. filter}}) (8760) + (x_{\text{other telemetry}}) (450)$$

From Section 6.1

$$x_T t_T = \left[(7.0) (8760) + (128.0) (450) \right] \times 10^{-6}$$

$$x_T t_T = 0.1190$$

SCTS Failure Rate

$$x_{SCTS} = \frac{x_C t_C + x_P t_P + x_R t_R + x_T t_T}{8760}$$

$$x_{SCTS} = \frac{0.3087 + 0.1130 + 0.0346 + 0.1190}{8760}$$

$$x_{SCTS} = \frac{0.5753}{8760} = 65.7 \text{ failures per million hours}$$

SCTS MTTF

$$MTTF = \frac{1}{x_{SCTS}} = \frac{10^6}{65.7} = 15,250 \text{ hours}$$

Probability of Successful Operation for One Year

$$R_{SCTS} = e^{-x_{SCTS} (8760)}$$

$$R_{SCTS} = e^{-0.5753}$$

$$R_{SCTS} = 56.2\%$$

6.5 Reliability Validation Test Program

Two types of reliability validation tests should be performed on the subject equipment:

6.5.1 MTTF Testing

The prototype Reflectometer Assembly, Power Subsystem, and Telemetry Package should be electrically connected as in the SCTS and subjected to the following mean-time-to-failure (MTTF) demonstration:

1. In the Environmental Laboratory, expose the assembled system to one cycle of simulated launch conditions of shock, vibration, and acceleration (using g-level data from past launches).

2. Subsequent to the simulated launch, place the equipment under test in a vacuum chamber (to simulate the orbital phase) for a time period of 2 months. During this interval, use a Solar Simulator to activate the solar panels and reflectivity specimens. Provide continuous monitoring of the transmitter and battery outputs.

   NOTE: By activating the command and telemetry systems more frequently than in the actual experiment, and by varying the light intensity more often than will occur in space, acceleration factors can be added which will equate the 2-month test period to 1 year of space operation.

3. Upon completion of step 2, repeat the launch cycle simulation of step 1.

REQUIREMENT:

Two failure-free launch cycles, plus a successful 2-month operating-life demonstration (accelerated to simulate 1 year of space time) shall serve to substantiate the MTTF prediction of Section 6.4.

6.5.2 WEAR-OUT Life Testing

The batteries, tungsten lamp, reflectometer drive motor, and reflectometer detector switch should be subjected to WEAR-OUT life

testing. Two each of these items should be activated until wear-out occurs (using an accelerated cycling rate).

NOTE: Vendor data may be used in lieu of the above testing, providing it is directly applicable to the SCTS application.

REQUIREMENT:

Each of these items shall demonstrate a wear-out life equal to at least 1.5 times the SCTS application.

6.6 Conclusions and Recommendations

The conclusions and recommendations which have evolved from the preceding reliability analysis are summarized below.

6.6.1 Orientation Subsystem

Cycle-life capabilities of the solenoid-activated valves and the centrifugal switch should be substantiated through testing.

6.6.2 Power Subsystem

1. Use HI-REL parts in all electronic circuitry.
2. Provide a redundant battery and a redundant string of solar cells.
3. Verify the cycle-life capability of the batteries by testing.
4. Add a parallel routing from the solar cells to the voltage regulators.

6.6.3 Environment Measurement Instrumentation

Emphasize the reliability of the rotary selector, its drive motor, and the power supply.

6.6.4 Reflectometer Subsystem

1. Use a redundant drive motor.
2. Verify the structural integrity of the reflectometer system by exposing it to a simulated launch.
3. Use HI-REL electronic piece parts throughout this subsystem.
4. Determine the WEAR-OUT life of the tungsten lamp, reflectometer drive motors, and detector commutator through testing.

6.6.5 Thermal Measurement Instrumentation
(Satisfactory as is.)

6.6.6 Telemetry Subsystem

1. Use HI-REL parts throughout this subsystem.

2. Consider on-board programmed activation of the Instrument and Telemetry Subsystems in case of a Command Channel malfunction.

3. The configuration for the Clock Oscillator should incorporate two cross-coupled solid-state multivibrators each employing internal redundancy.

4. Hi-level data should not be attenuated and routed through the Signal Amplifier, but rather should be fed directly into the Analog-to-Digital Converter in parallel with the Signal Amplifier output.

5. The transmitted data format should be such that the most significant bit (MSB) of each word is transmitted first, so that failures in the A/D Converter and Parallel-to-Serial Converter will not necessarily destroy data transmission capability.

6. The telemetry Transmitter should be completely solid state with protection against power transients introduced by the power programming circuitry.

6.6.7 Assembled SCTS

Conduct a reliability validation test by exposing the prototype Reflectometer Assembly, Power Subsystem, and Telemetry Subsystem to two cycles of simulated launch conditions and two months of accelerated life testing. Of importance, should be the effect of repetitive activations of the various subsystems.

6.6.8 Probability of Success

With the inclusion of the redundant elements proposed herein, the probability that the SCTS will operate successfully for

1 year is 56.2 percent. As indicated by the mathematical computations, a substantial portion of the overall SCTS failure rate is contributed by the Command Receiver and Command Decoder. This area should be investigated first if a higher probability of mission success is desired.

7. SEPARATION OF EFFECTS

The results of a previous study of the reflective surfaces flight experiment on Contract NAS1-2880 (Ref. 1) indicated the two aspects of the space environment most likely to degrade reflective surfaces were micrometeoroids and low energy protons. Therefore, during the present contract, these two environmental factors have been studied in more detail, with particular emphasis on devising techniques to separate their effects from one another in the flight experiment. The present investigation, which is reported below, leads to the conclusion that it is extremely difficult to achieve a sharp separation of micrometeoroid and proton effects, within the boundary conditions of a single, reliable, and relatively simple flight experiment. However, a method which would yield a partial separation of effects is discussed.

Additional material on the space environment, not included in Ref. 1, is presented below. Following this, the techniques of effects separation are discussed and evaluated.

7.1 Space Environment: Micrometeoroids

Three features of the micrometeoroid environment are discussed here to supplement the results reported in Ref. 1. These are (1) an apparent altitude dependence of the flux, (2) discrepancies between data from impact (microphone) detectors and data from penetration detectors, and (3) directionality of the meteoroid flux.

Micrometeoroid flux measurements from various satellites and space probes are plotted as a function of altitude in Fig. 7-1. The "altitude" is taken to be the arithmetic mean of apogee and perigee for the orbital vehicles and, in the case of Mariner II, is taken to be the mean altitude during the 950-hour sampling period. Since the mass sensitivities are different in each of the measurements, the flux rates have been normalized to a mass sensitivity of 1×10^{-8} g, by use
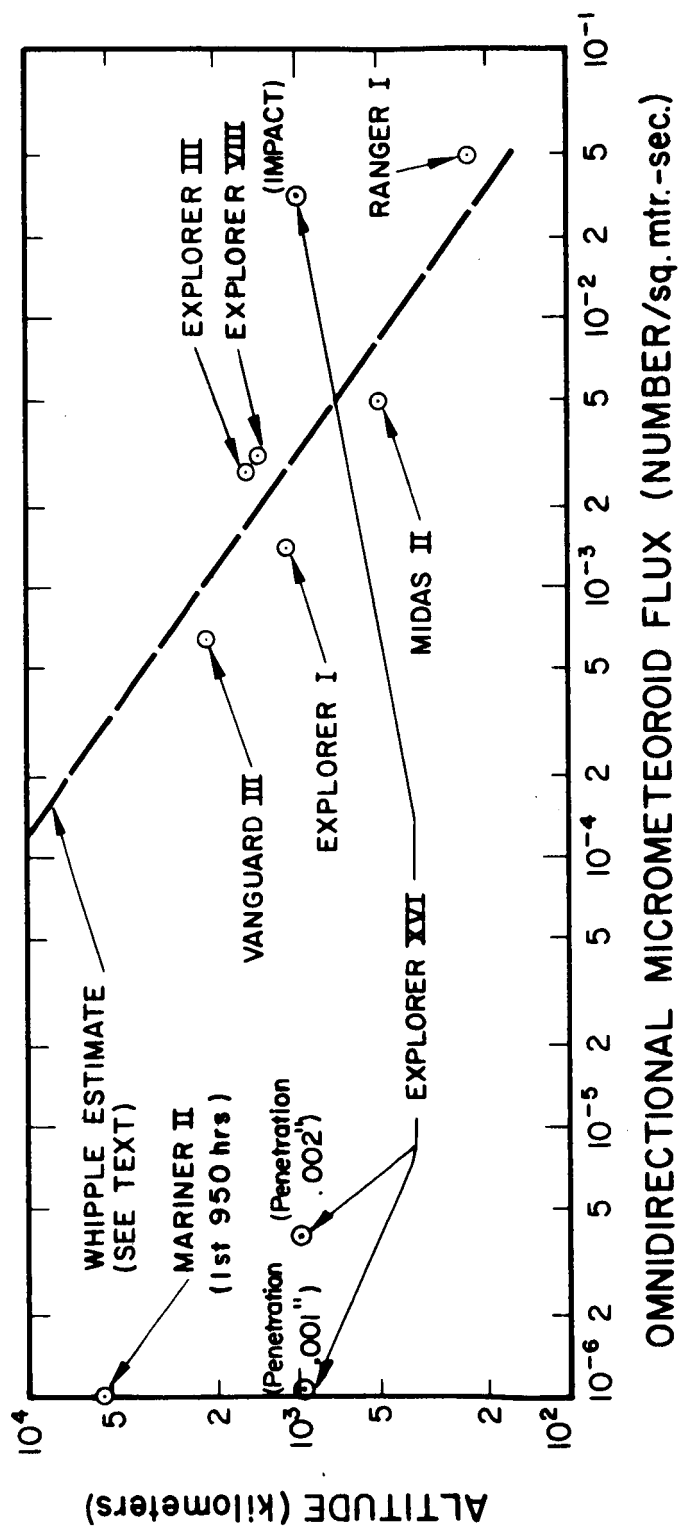
FIG. 7-1 OBSERVED VALUES OF MICROMETEOROID FLUX VS ALTITUDE

of the approximation that the cumulative flux of micrometeoroids of mass $\geq$ m is proportional to m^{-1}. Although both the altitude assignment and sensitivity normalization procedures may introduce some error, it is believed the validity of the general results is not affected.

It is seen in Fig. 7-1 that most of the data points fall along a straight line in the log-log presentation. This line (shown dashed in Fig. 7-1) is of the form:

$$\text{Flux} = (\text{constant}) \times (\text{altitude})^{-1.4},$$

which form was first suggested by Whipple (Ref. 2) based on early satellite observations and zodiacal cloud calculations. The Mariner II results suggest the flux decrease may be an even stronger function of altitude.

The other outstanding feature of the data in Fig. 7-1 is the large discrepancy between the fluxes measured by the impact detector and the penetration detectors on Explorer XVI. It should be noted that all other measurements displayed in Fig. 7-1 were made with impact detectors, except in the case of Explorer III, where wire grids were used.

The question of the reliability of impact detector measurements was recently discussed by Hastings (Ref. 3):

> "A characteristic of the Explorer XVI impact data is the high counting rates observed in the high- and low-sensitivity impact detection systems in the first few days of orbit, and particularly evident in the high-sensitivity system. Such an effect has been observed on a similar experiment on a satellite of this type (Explorer XIII, unpublished data) and on other satellite impact experiments, but the mechanism of the effect is not well understood. It is hypothesized that the initially high counting rates may be due to debris in the near vicinity of the satellite structure remaining from the ascent and injection into orbit, and which are temporarily loosely entrapped within the satellite structure; outgassing of elements of transducer arrays; thermal and/or mechanical strain relief "settling" effects; and so on.
>
> A basic question with regard to the microphone-type impact experiments in general is the validity of the assumption that momentum response at hypervelocity

meteoroid encounter is the same as, or even comparable
with, the observed momentum response of such systems
at the low velocities employed for calibration."

If further space measurements confirm present evidence that
impact detectors are giving erroneously high flux rates, estimates of
the hazard to reflective surfaces from micrometeoroids will have to
be sharply revised downward. In this connection, recent measurements
on the Echo I aluminized Mylar satellite have indicated a degradation
of specular reflectivity of about 2 percent per year (Ref. 4). This
small amount of degradation would certainly not impair the operation
of most solar concentrator systems.

A final point of interest is the question of directional
properties of the micrometeoroid flux which might be used to expose
various samples to differing fluxes by means of orientation. This
apparently would not be a useful technique since Davidson and Sandorff
(Ref. 5) have indicated that the flux is approximately isotropic with
respect to direction, as a result of the Earth's being immersed simul-
taneously in many individual meteoroid streams.

7.2   Space Environment: Low Energy Protons

There have been no new data which significantly change the
picture of the proton space environment presented in Ref. 1. In par-
ticular, there is still a lack of detailed data on low energy protons
(E_p < 100 kev). Unfortunately, this is exactly the energy range of
interest with respect to reflective surface degradation, as is shown
at the end of this section. Therefore, in the material presented
below, it is possible to review the present state of knowledge of low
energy protons in space, indicating gaps and conflicts where they exist.

Based on several geophysical arguments, no significant flux of
low energy protons would be expected in the vicinity of the Earth, i.e.,
up to 1×10^4 km altitude. The solar wind protons, the energy of which
ranges from a few electron volts to a few hundred electron volts, are
excluded from the Earth's magnetosphere by magnetic deflection. The
proton source currently believed to be of most importance, beta decay

of albedo neutrons, produces mostly high energy protons. Even if a source of low energy protons could be hypothesized, the buildup of a large flux would be severely limited by the short lifetimes experienced by these protons at altitudes below 1×10^4 km (Ref. 6).

The results of Davis and Williamson (Ref. 7), which were obtained from Explorer XII data, tend to confirm this latter theory. Proton spectra were measured at altitudes of 1.1×10^4 km, 2.5×10^4 km and 3.3×10^4 km for the energy range 100 kev $< E_p <$ 1 Mev. For the lowest altitude, the proton flux showed a sharp decrease below 300 kev, while at the higher altitudes the flux remained large down to the lower end of the measured range (100 kev). Bader (Ref. 8) attempted to measure the very low energy proton spectrum (100 ev $< E_p <$ 20 kev) with another instrument on Explorer XII. He detected no protons in this energy range in the region of 300 km to 77,300 km altitude. The threshold sensitivity of the instrument was 3.1×10^6 protons/cm^2/sec/sr.

In possible conflict with the above results are the data from an Injun I experiment which are presented by Freeman (Ref. 9). Proton fluxes as high as 3×10^8 protons/cm^2/sec/sr for the energy range 500 ev $< E_p <$ 500 kev was measured at about 1000 km altitude. Since proton lifetimes are extremely short at this altitude, it is difficult to postulate a proton source strong enough to produce this magnitude of flux, as was pointed out by Freeman himself (Ref. 9). Thus far, no other measurements have been made at this altitude and in this energy range. Many reviewers of radiation belt data have mentioned Freeman's results, but none have attempted to give a physical interpretation of them.

The spatial and angular distributions of the protons also are of interest in this study. As is well known, the fluxes are most intense in the vicinity of the geomagnetic equator, decreasing to essentially zero in the polar regions. There is also a strong angular dependence of the flux distribution with respect to the magnetic field lines. Typical experimental results (Refs. 7 and 9) have shown an

increase in flux of several orders of magnitude when going from 0° to 90° (to $\vec{B}$) with a collimated proton detector. This is the angular dependence that may be expected, since, although the generation (or injection) of protons in the magnetic field is isotropic, the recombination rate for the protons increases as the proton mirror point decreases in altitude, and the mirror points are lowest for low-angle protons.

The concern with the proton environment with respect to reflective surface degradation is related to the possibility of sputtering, as indicated in Ref. 1. The reason for emphasis on the low energy portion of the proton spectrum is that these are the protons most likely to cause sputtering. This is a direct result of the fact that the energy dissipation per unit distance, dE/dx, for charged particles in any material increases as the energy, E, of the particle decreases. To demonstrate this fact in a quantitative manner, Fig. 7-2 was plotted showing dE/dx vs. E for protons in aluminum. Unconventional units were chosen for dE/dx (ev/atomic diameter of aluminum) because these are more meaningful in discussing sputtering physics than the usual units, Mev/cm. It appears reasonable to assume that a specific minimum energy, dE_{min}/dx, must be dissipated within one atomic diameter in order to remove an aluminum atom. This quantity, dE_{min}/dx, may be thought of as the energy required to overcome the bonding forces on the atom, or as the energy required to ionize the atom. For example, if it is assumed that the aluminum must be triply ionized to effect sputtering, dE_{min}/dx must be 28.3 ev/atomic diameter (see ionization potentials plotted on Fig. 7-2). This, in turn, implies that only protons with energies below 0.2 Mev will cause sputtering. There is empirical evidence that dE_{min}/dx may be even higher; for example, Holland (Ref. 10) quotes results showing the threshold energy for sputtering aluminum with Hg+ ions is 120 ev. Although the exact dE_{min}/dx is not known for proton sputtering of aluminum, it is clear from the above discussion that only the low energy portion of the proton spectrum is likely to cause sputtering.
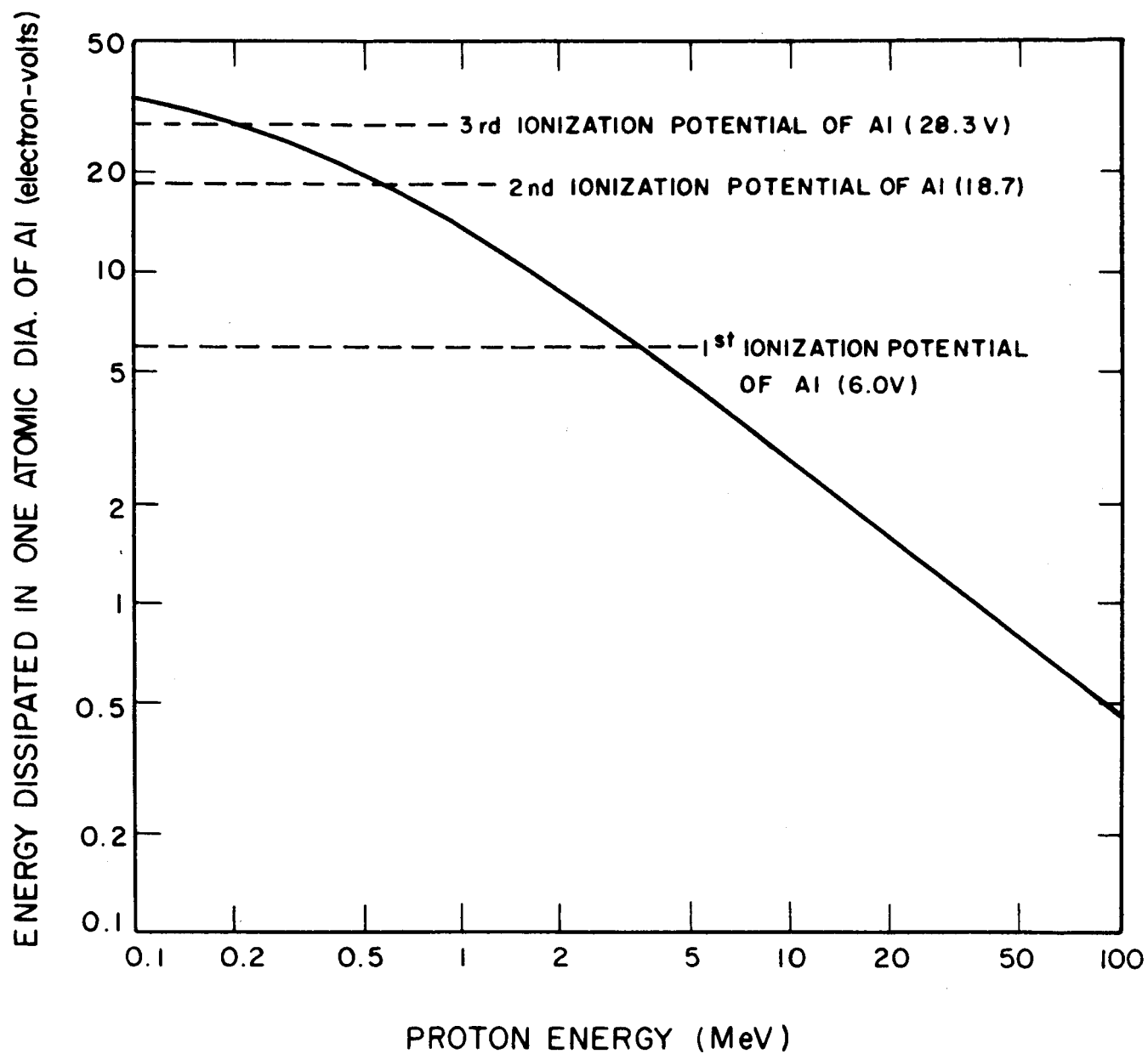
FIG. 7-2 ENERGY DISSIPATION PER UNIT LENGTH IN Al VS PROTON ENERGY

73612923

7.3 Techniques for the Separation of Effects

For convenience of discussion, the methods investigated to separate micrometeoroid and proton effects are divided into two categories: physical methods and spatial methods. Physical methods are those in which something is done at or near the reflective surface sample to give it selective exposure to only one of the two environmental components of interest. Spatial methods are those using sample orientation or choice of orbit which would give the selective exposure.

7.3.1 Physical Methods

Two specific physical methods for separating the degradation effects of micrometeoroids from those of low energy protons were studied. They are: (1) electrostatic shielding of some samples from protons by continuous application of a high positive potential to these samples, and (2) covering some samples with a thin membrane, e.g., 1/4 mil Mylar, which might give significantly greater attenuation of low energy protons than of micrometeoroids.

The electrostatic shielding method has several desirable features. It would operate only on protons, leaving exposure to the rest of the environment unchanged, except for a slight increase in incident electron energies. The power consumption would be quite low, since even in intense charged particle fluxes, the current drain would be of the order of 1×10^{-12} amperes. The high-voltage, low-current power source might present some problems; however, it is likely that a source such as radioisotope batteries could be used.

There are serious defects in this method. It is doubtful whether a voltage of greater than 10 to 20 kv could be reliably and continuously applied to the samples in this long term experiment. Since the literature indicates that within the magnetosphere the flux of protons with energy less than 20 kev is small compared with those of somewhat higher energy, e.g., 0.1 to 5 Mev, it would appear that little advantage would be gained by electrostatic shielding. If so, the net result might be an increase in the damaging effects of the protons,

since those of sufficient energy to penetrate the field would be reduced
in kinetic energy and might be more efficient in sputtering (as discussed
in Section 7.2). Present knowledge of the proton environment will not
allow prediction of the effects of electrostatic shielding with suffi-
cient confidence to justify use of this method.

The membrane cover method was suggested by the fact
that micrometeoroids possess a vastly larger kinetic energy per particle
than do protons. For example a micrometeoroid with mass of 1×10^{-10} g
traveling at a velocity of 22 km/sec has a kinetic energy of 1.5×10^{13}
ev, compared with proton energies of 1×10^{5} ev. It was hoped, there-
fore, that a suitable membrane would stop low-energy protons while pass-
ing the micrometeoroids essentially unattenuated. However, this proved
not to be the case. It was determined that while 1/4 mil Mylar would
stop protons below 400 kev, it would also stop micrometeoroids with mass
below about 1×10^{-9} g. This latter figure is based on the reported
mass sensitivity of the Mylar film - CdS cell micrometeoroid detectors
carried on Explorers VII and XVI. It is apparent that the energy ab-
sorption in the membrane for micrometeoroids is so much stronger than
for protons that the desired separation of effects could not be ac-
complished.

7.3.2 Spatial Methods

Certain spatial methods for effects separation look
more promising than those discussed above. These spatial methods take
advantage of the strong dependence of the proton flux upon geomagnetic
latitude and upon direction with respect to the magnetic field lines,
in conjunction with the relative independence of the micrometeoroid
flux with respect to these parameters.

Orientation of two sets of samples on the payload,
such that one set faced in a direction at 90° to the magnetic field
while the other set faced in the direction of the field, would give
a large difference in proton exposure to the two sets. It also would
be necessary to have the samples recessed in their holders so that the

acceptance cone angle would be, say, 30 degrees. In this manner, one set would accept protons with pitch angles of 75 to 105 degrees, while the other set would accept protons with pitch angles of -15 to +15 degrees. This would lead to a difference in exposure factor of 10 to 100 (see Section 7.2).

Some difficulties would be encountered in arranging and preserving the required sample orientations. For example, assume a flat cylindrical payload in a near-equatorial orbit, with one flat side (on which most samples are mounted) oriented toward the sun. In this case the flat-surface samples would be oriented at very nearly 90 degrees to the magnetic field. This would require that the 0-degree samples be mounted on the north and south of the circular wall of the payload. This would probably mean that a separate reflectometer would be needed for these samples. Also, spin stabilization of the payload would not be permitted. In addition the 0-degree samples would not be directly exposed to solar radiation. Despite these disadvantages, this method or some modification of it may prove useful in strongly reducing the proton exposure on some samples.

A more straightforward spatial method for effects separation is the choice of an orbit in which the peak proton flux and the peak micrometeoroid flux occur in different portions of the orbit. By means of a movable shield, one set of samples can be given more proton exposure while another set is given more micrometeoroid exposure.

An example of a desirable "separation-of-effects" orbit might be an elliptical polar orbit with its apogee at about 12,000 km over the equator, in the heart of the proton belt; and with its perigee at about 500 km over the poles, where the proton flux is negligible and the micrometeoroid flux is probably quite large.

The movable shield could be simply arranged by attaching metal plates to both sides of the reflectometer arm so as to shield one or two samples on each side of the arm's "stop" position. By providing two "stop" positions and a means for moving the arm from one

position to the other at appropriate orbital positions, the selective exposure of the two sets would be accomplished. Several means are available for moving the arm at the correct time, e.g., ground command, an on-board sequencer, or a proton detector system which would expose the proton samples when a specified flux level was exceeded and expose the meteoroid samples when the flux fell below this level.

The spatial method discussed above appears to be the most useful for a clear separation of effects. The only disadvantage is that in a polar-orbiting vehicle, a somewhat longer time would be required to get a specified proton dose. If the separation of proton and micrometeoroid effects is deemed to be of primary importance in this experiment it is strongly recommended that the selective-exposure-orbit method be considered.

REFERENCES

SECTION 7

1. Final Report, "Study of a Flight Experiment of Solar-Concentrator Reflective Surfaces", Contract NAS1-2880, Electro-Optical Systems, Inc., EOS Report 4100-Final (1 November 1963).

2. F. L. Whipple, "The Dust Cloud About the Earth", Nature 189, 127-128 (1961).

3. E. C. Hastings, Jr., "The Explorer XVI Micrometeoroid Satellite, Supplement III", NASA Technical Memorandum TM X-949, pp. 13-14 (March 1964).

4. "Photometric Measurements of Surface Characteristics of Echo I Satellite," Goodyear Aerospace Corp. GER 11648 June 19, 1964, Contract NAS1-3114.

5. J. R. Davidson and P. E. Sandorff, "Environmental Problems of Space Flight Structures: II. Meteoroid Hazard", NASA Technical Note D-1493, p. 7 (January 1963).

6. H. Liemohn, "The Lifetime of Radiation Belt Protons with Energies Between 1 Kev and 1 Mev", J. Geophys. Research, 66, 3593-3595 (1961).

7. L. R. Davis and J. M. Williamson, "Low Energy Trapped Protons", Space Research III, (W. Priester, ed.), John Wiley & Sons, Inc., New York (1963).

8. M. Bader, "Preliminary Explorer XII Data on Protons Below 20 Kev", Space Research III, (W. Priester, ed.), John Wiley & Sons, Inc., New York (1963).

9. J. W. Freeman, "Detection of an Intense Flux of Low-Energy Protons or Ions Trapped in the Inner Radiation Zone", J. Geophys. Research, 67, 921-928 (1962).

10. L. Holland, "Vacuum Deposition of Thin Films", p. 409, John Wiley & Sons, Inc., New York (1958).